Constraints on the Very Faint X-Ray Transient System M15 X-3

by

Robin Arnason

A thesis submitted in partial fulfillment of the requirements for the degree of

Master of Science

Department of Physics
University of Alberta

Abstract

We present the first combined optical/X-ray observation of a very faint transient X-ray binary (VFXT), M15 X-3. *Chandra* observations constrain the source to be $< 10^{34}$ erg s^{-1} in all observations. The X-ray spectrum shows evidence of curvature, and is best fit by a broken power law with break energy $E_{break} = 2.71^{+0.38}_{-0.05}$ keV, and power law indices of $\Gamma_1 = 1.25^{+0.02}_{-0.01}$ and $\Gamma_2 = 1.82^{+0.20}_{-0.02}$. Fitting the *HST* magnitudes of the optical counterpart suggests a power-law accretion disk and a main-sequence companion of size $0.440^{+0.035}_{-0.060}\ M_{\odot}$. This mass estimate is likely to be an upper limit since the short inferred period of $P \lesssim 4$ hr implies the companion is irradiated. This rules out several explanations for very faint transient behaviour for this source, and suggests a neutron star accretor experiencing inefficient accretion due to a propeller effect.

Preface

Some of the research conducted for this thesis forms part of an international research collaboration. This collaboration includes Professors Craig Heinke and Gregory Sivakoff at the University of Alberta, Professors Haldan Cohn and Phyllis Lugger at Indiana University, and myself.

The literature review in Chapter 1, data reduction and analysis in Chapter 2, model fitting in Chapter 3, and conclusions in Chapter 4 are my original work. Interpretation of the data available on M15 X-3 was done in consultation with Gregory Sivakoff and Craig Heinke.

In the course of this research I reduced and analyzed publicly available *Chandra* archival data, where the majority of the observations were originally taken for other scientific reasons than are presented in this thesis. For ObsIDs 1903, 2412, and 2413 the PI was Phillip Charles. For ObsIDs 11029, 11886, and 11030 the PI was Andrea Dieball. For ObsIDs 9584 and 13710 the PI was Craig Heinke, with the latter ObsID originally taken for the primary scientific reasons discussed in this thesis. For ObsID 13420 the PI was Gregory Sivakoff. I performed data reduction and analysis using the publicly available software packages CIAO, HEAsoft, and XSPEC.

I also used three publicly available *HST* observations in the course of this research, where two of the observations were originally taken for other scientific reasons than are presented in this thesis. The latter observations include Proposal IDs 5742, where the PI was James Westphal, and 9039, where the PI was Bernard McNamara. Observations from ProposalID 12751, where the PI was Craig Heinke, were originally taken for the primary scientific reasons discussed in this thesis. For all of these observations, Haldan Cohn and Phyllis Lugger reduced the data and calculated the magnitudes of the stars in M15 (including M15 X-3). I utilized their

provided magnitudes to model the M15 X-3 system using the publicly available PYSYNPHOT software package. With this package I created a python script that fit these magnitudes to a variety of models from the Castelli-Kurucz library of stellar atmospheres.

“I made a fire and watching it burn / I thought of your future / With one foot in the past now just how long could it last?”

Tears For Fears

”Head over Heels" (1985)

Acknowledgements

This work could not have been accomplished without the guidance, support, and assistance of many of my colleagues, friends, and faculty.

I would like to thank the members of my committee, especially my supervisor Gregory Sivakoff, as well as Craig Heinke, Sharon Morsink, and Darren Grant. Their guidance and insights were invaluable in the completion of this work.

I also owe thanks to the other faculty members at the University of Alberta who helped educate me and develop my abilities as a physicist: Dmitri Pogosyan, Kevin Beach, Richard Sydora, Erik Rosolowsky, Natasha Ivanova, Alexander Penin, and others.

I would like to thank my collaborators at Indiana University (IU), Haldan Cohn and Phyllis Lugger, who reduced the *HST* data and provided me with the magnitudes, without which this work would not be possible.

I would also like to thank all of my friends and colleagues who helped support me as I completed this work: Arash Bahramian, Alex Tetarenko, Bailey Tetarenko, Kaylie Green, Khaled Elshamouty, Jose Luis Avendano Nandez, Alice Koning, Abigail Stevens, Dario Columbo, Nathan Leigh, Jeanette Gladstone, Sarah Nowicki, Tania Wood, Megan Engel, Andrei Catuneanu, Stephen Portillo, Reggie Miller, and others.

I would like to thank my close family for being supportive in helping me pursue my career as a physicist: Arne Arnason, Sandra Kram, Holly Arnason, Mathilde Kram, Albert Arnason, and Jesse MacVicar.

I also acknowledge the financial support of the University of Alberta and the Queen Elizabeth II Master's Scholarship in completing my degree.

Contents

List of Tables

List of Figures

List of Abbreviations

Chandra	Chandra X-ray Observatory
HST	Hubble Space Telescope
eV	electronVolt, 1.6×10^{-19} Joules
keV	kilo-electronVolts
pc	parsec (3.086×10^{16} m)
kpc	kiloparsec
erg	CGS unit of energy (10^{-7} J)
$M_\odot$	solar mass (1.9891×10^{30} kg)
$R_\odot$	solar radius (6.955×10^{8} m)
"	arcsecond (1/3600th of a degree)
‘	arcminute (1/60th of a degree)
XRB	X-ray binary
NS	Neutron star
BH	Black hole
WD	White dwarf
LMXB	Low-mass X-ray binary
HMXB	High-mass X-ray binary
VFXT	Very faint X-ray transient
MSP	Millisecond pulsar
G	gravitational constant (6.67384×10^{-11} m^3 kg^{-1} s^{-2})
σ	Stefan-Boltzmann constant (5.670×10^{-8} W m^{-2} K^{-4})
k or k_B	Boltzmann constant (1.380×10^{-23} J K^{-1})
GC	Globular cluster
CMD	Color-magnitude diagram
h	Planck constant (6.626×10^{-34} J s)
χ^2	chi-square statistic
Jy	jansky, unit of flux density (10^{-23} erg s^{-1} cm^{-2} Hz^{-1})

Chapter 1

Introduction

1.1 X-Ray Binaries

1.1.1 Low-Mass X-Ray Binaries

Since the identification of X-ray pulsars by the first X-ray satellite *Uhuru*, it has been known that the majority of the brightest X-ray objects in the sky are X-ray binaries (XRBs). These relatively rare astronomical objects consist of a compact object (neutron star (NS) or a black hole (BH)) that pulls material away from a companion star via a process known as *accretion* [1, 2]. Broadly, XRBs can be split into two categories, separated by the mass of the companion: the low-mass (LMXBs) and the high-mass (HMXBs) [1]. The key distinction between these two categories, aside from the companion mass, is the mechanism by which accretion occurs. For LMXBs, accretion typically occurs when the companion has expanded to fill its Roche Lobe, the surface of gravitational potential at which material is bound to the star (see Figure 1.1). Material flows from the companion to the primary object through the L_1 Lagrangian point of the system, the location at which the gravitational force from each star is the same. By contrast, HMXBs are typically powered by strong mass loss in the form of wind from the companion. Since the companions in LMXB systems are not massive enough to drive strong winds, they will typically ac-

crete strongly when the LMXB has filled its Roche Lobe. The X-rays themselves are produced by a variety of processes in the binary system, including *Bremsstrahlung* when the material falls onto the surface of the compact object, inverse Compton scattering by electrons around the compact object, blackbody-type emission from either the compact object or the disk of accreted material around it, line emission from heavy atoms with hydrogen-like and helium-like electron configurations, or synchrotron emission from electrons accelerated relativistically in magnetic fields [3]. Regardless of the details of the process, the primary energy source is the release of gravitational energy as material falls onto the surface of the compact object. For an object of mass m falling onto an object of mass M and radius $R_\star$, the amount of energy released per gram is given by [3]:

$$E_{release} = \frac{GMm}{R_\star}. \tag{1.1}$$

For a typical neutron star, $M = 1.4M_\odot$ (where $M_\odot$= 1 solar mass, roughly 1.99×10^{30} kg) and $R_\star = 10$ km, this leads to an energy release of approximately 10^{20} erg g^{-1}. The regime of radiation emitted by this process is bounded by two temperatures. At the lower limit, if all the energy released were radiated as a blackbody spectrum, its temperature would be:

$$T_b = \left(\frac{L_{acc}}{4\pi R^2 \sigma} \right)^{1/4}, \tag{1.2}$$

where L_{acc} is the accretion luminosity (typically of order 10^{36-38} for neutron stars), and σ is the Stefan-Boltzmann constant. For typical neutron star values, $T_b \approx 10^7$ K, or (multiplying by the Boltzmann constant k) $E_b \approx 1$ keV. The upper bound is determined in the case where all of the energy is converted to thermal energy. In this case, the temperature is found by setting the thermal energy $3kT$ equal to the potential energy $\frac{GMm_p}{R_\star}$, which solves to give [3]:

$$T_{th} = \frac{GMm_p}{3kR_\star}. \tag{1.3}$$

Note that we treat accretion as the infall of individual proton and electron pairs (since the accreted material is typically hydrogen), with $m = m_p + m_e \approx m_p$. For typical neutron star values this gives $T_{th} \approx 10^{11}$ K, or $E_b \approx 60$ MeV. We would therefore expect the radiation emitted by accreting neutron stars to range between 1 keV and 50 MeV, making them X-ray to gamma ray emitters.

Depending on the nature of the compact object, between 7 and 10 percent of the rest mass of the infalling matter is converted to X-rays, making accretion in X-ray binaries one of the most efficient energy-generation processes in the Universe, exceeding the efficiency of nuclear burning by hydrogen by a factor of roughly 20-80 [3]. Since the material being accreted by the compact object possesses angular momentum (from the rotation of the donor star), in general it is not possible for material to fall directly onto the surface of the compact object. Instead, conservation of angular momentum leads to material accreting through (near-)circular orbits, forming an object known as an *accretion disk*. The emitted spectrum of an accretion disk is discussed more in Section 1.1.3. It is noted that accretion disks are an essential component in the interpretation of XRB systems, where the effects on the observed behaviour of LMXBs are dramatic.

The development of progressively more powerful X-ray detectors has revealed that most LMXBs are *transient*. Many of these systems are observed to spend long periods of time (months to years) in *quiescence*, accreting at a very low rate with a low X-ray luminosity, before experiencing short periods (days to weeks) of outburst, where their spectral energy distribution changes and their luminosity can increase by up to a few orders of magnitude. This behaviour is generally believed to be caused by instabilities in the accretion disk itself, in particular where the accretion disk's temperature fluctuates around that for hydrogen ionization. Two timescales are necessary to discuss this instability. The first is the *thermal timescale*, which reflects the time that it takes for the system to radiate energy and return to thermal equilibrium. For material in the disk moving at velocity v and at radius R from the accreting object of mass M with a local sound speed of c_s, the thermal timescale is

roughly given by [3]:

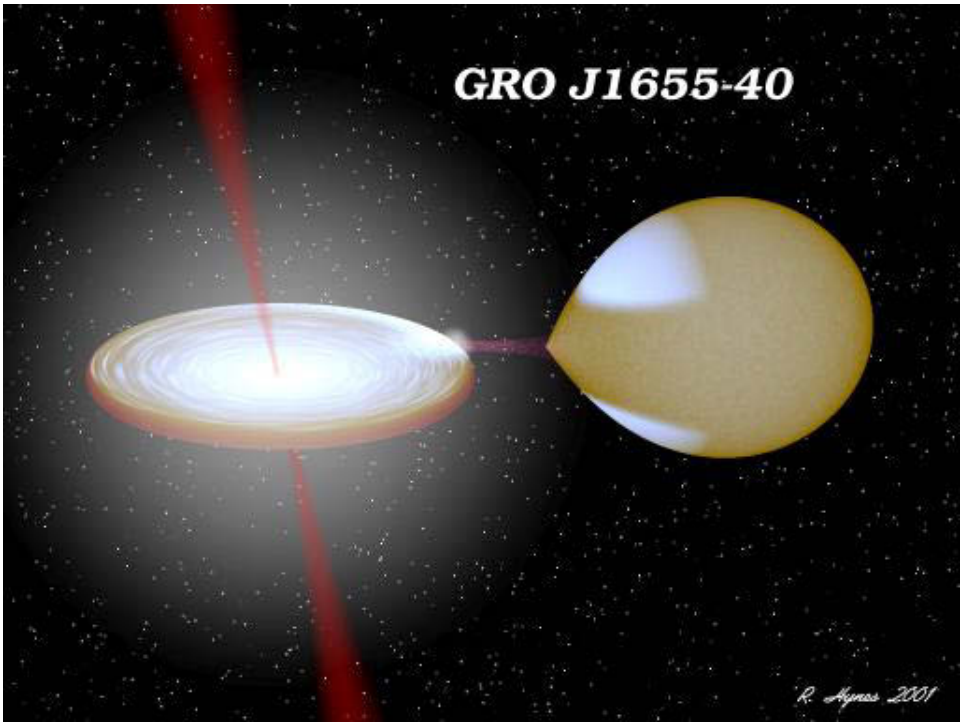

Figure 1.1: Artist's impression of the black hole X-ray binary GRO J1655-40. On the right, a star of $\approx 2\ M_\odot$ has filled its Roche Lobe, as is evidenced by the teardrop shape of the star close to the primary. An accretion stream in the middle indicates that material is being transferred from this companion to a compact object, forming an accretion disk on the left. At the centre of the accretion disk, matter falls onto the surface of an $\approx 7\ M_\odot$ black hole. Additionally, this picture depicts the presence of radio-bright jets radiated from the black hole at a nearly perpendicular angle from the orbital plane of the system. These powerful plasma jets contain relativistic particles that can remove some angular momentum from the system. Image credit: Robert Hynes.

$$t_{thermal} \approx \frac{R^3 c_s^2}{GMv}. \tag{1.4}$$

For typical disks (located around a mass $\approx 1\ M_\odot$ with accretion rates of order 10^{16} g s^{-1}, and characteristic disk size 10^{10} cm), the thermal timescale tends to be of order minutes. This is much shorter than the timescale of matter moving through the viscous accretion disk, known as the *viscous timescale*, which tends to be of order

days to weeks, and is given roughly by [3]:

$$t_{viscous} \approx \frac{R}{v}. \tag{1.5}$$

Since the thermal timescale is shorter than the viscous timescale, the material in the disk must continually radiate the potential energy gained as it moves inwards. The disk should therefore radiate away half of the energy gained by matter falling onto the compact object. For a neutron star accretor the remaining energy should be radiated at the NS surface, whereas for a black hole this energy loss occurs at the event horizon.

From the above timescales, the disk instability can be described as follows [4], with a graphical representation in Figure 1.2:

1. In quiescence, material slowly builds on the disk at low levels, leading to an increase in density, and hence an increase in pressure, resulting in an increase in the local disk temperature on viscous timescales.

2. When a portion of the disk reaches a temperature $T_{\text{local}} \approx T_{\text{H ionization}}$, hydrogen in the disc will become ionized, resulting in magnetic fields being trapped in the disk, and fixing the charged particles to the field lines. This causes nearby particles to spread apart, with particles closer to the inner edge of the disk falling inward faster and particles closer to the outer edge of the disk slowing down. The effect of this process (known as the magneto-rotational instability) is to increase the accretion rate, with a wave of heat propagating through the disc on thermal timescales [5].

3. The compact object will accrete at this high rate, consuming the disk until the outer portion of the disk falls below the hydrogen ionization temperature.

4. A cooling wave moving inward through the disk on viscous timescales will “shut off" the high accretion rate and the system will return to quiescence.

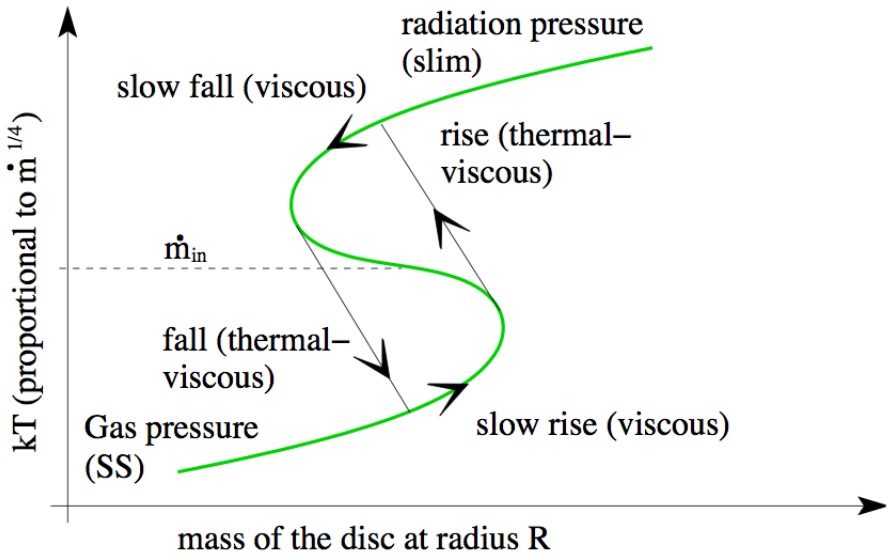

Figure 1.2: Plot of the hydrogen ionization instability at a local point within an accretion disk. As mass builds at a particular radius on the viscous timescale (slow rise), that portion of the disk begins to increase in temperature. Once the critical temperature regime for hydrogen ionization has been exceeded (marked by the accretion rate $\dot{m}_{in}$), the accretion rate of the disk will rapidly increase (rise), and a heat wave will propagate through the disk on the thermal timescale. The accretion disk will then be eroded on the viscous timescale (slow fall). As material is consumed at this radius, pressure and temperature are reduced until the ionization temperature is reached. At this point, the disk "switches off" (fall) on the viscous timescale, with a cooling wave being triggered at the edge of the disk and moving inward, until hydrogen is again neutral. After this, the process repeats. This figure is reproduced from Done et al. (2007) [6].

For NS and BH binary systems, the final step tends to proceed much more slowly (compared with WD systems, for which this model was originally developed), since irradiation from the compact object can maintain higher temperatures in the inner portions of the disk for longer periods of time [6, 7]. Observationally, this transient cycle tends to manifest itself for a neutron star accretor, in quiescence to have observed soft (low energy) X-ray spectra due to surface emission from the neutron star and/or emission from the accretion disk [8]. During outburst, a hard (high en-

ergy) component tends to dominate emission [9], and is sometimes accompanied by a softer component due to emission from the neutron star surface. The hard component is likely to be emission from a hot corona of inverse Compton-scattered electrons surrounding the compact object itself. These observational features form the motivation for the X-ray spectral fitting of M15 X-3 shown in Section 2.1.4.

1.1.2 Globular Clusters and M15

LMXBs are detected throughout the Milky Way, but are observed to be much more abundant per mass (by a factor of roughly 100) in the Galactic globular clusters (GCs) compared to within the Milky Way proper [10, 11]. In general, LMXBs are the end products of standard binary evolution. However, it is generally believed that the abundance of LMXBs in the GCs is in part due to formation through dynamical interactions, efficiently produced in the dense cores (the central density of a globular cluster can reach a million times the local stellar density near Earth). Aside from a relative LMXB abundance, GCs are extremely useful in X-ray observations for a number of reasons:

1. They are extremely old and have one (or perhaps a few) stellar populations. The lack of many epochs of star formation is attributed to supernovae from short-lived high-mass stars that clear the gas necessary for star formation from the cluster early in the cluster's lifetime. Globular cluster ages can be reasonably determined from the point where the main sequence of stars turns into the sub-giant branch in a colour-magnitude diagram of the GC. The presence of multiple populations and age-metallicity degeneracy is a complication. An example of the main-sequence and white dwarf sequence of two GCs is given in Figure 1.3.

2. By fitting the track of the GC stars through the colour-magnitude diagram (CMD) against known stellar populations, GC distances can be determined with low relative error, typically within about 6% [12, 13].

3. Globular clusters, especially ones at high Galactic latitude, tend to have relatively little scattering due to interstellar dust and absorption due to interstellar gas when compared with objects located in the plane of the Milky Way (especially objects located in the direction of the Galactic Centre).

4. As mentioned above, their high central densities make them extremely efficient at forming LMXBs.

In addition to being efficient at forming LMXBs, globular clusters can have their structure altered by the presence of binaries, potentially even supplying enough kinetic energy in their formation to alter the size of the core, and reversing the core collapse [14]. The study of LMXBs in globular clusters may therefore also probe the evolution of the host cluster.

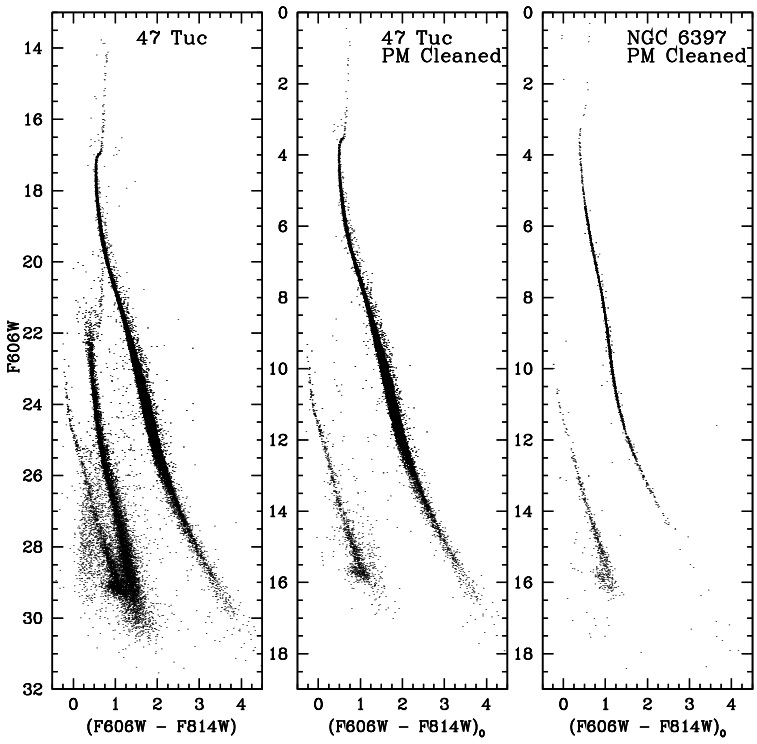

Figure 1.3: Colour-magnitude diagrams of the globular clusters 47 Tucanae and NGC 6397. Magnitude (vertical axis) measures the brightness of the object (often in the V filter), where lower magnitude objects are brighter. Color is determined by subtracting the magnitude in one filter from the magnitude in another, and is a proxy of the temperature of an individual object. In these images, the magnitude is measured in F606W, a broad V-band filter. Color is obtained by subtracting F814W, a broad I-band filter, from the V filter. Several features of the cluster population are represented. The long black band of points on the right of each panel represents the "main sequence" of each cluster, the population of stars in the cluster undergoing normal stellar evolution. The smaller, fainter track along the left of each image represents the white dwarf cooling sequence, the track along which white dwarfs cool as they age. In the left panel, an additional track occurs between the main sequence and the cooling sequence - these are stars from the Small Magellanic Cloud (SMC) that are contaminating the frame, as the SMC is very close to 47 Tuc on the sky. The middle panel shows 47 Tuc's CMD after the SMC stars have been removed using the proper motion of these objects. NGC 6397's CMD, also with contaminating stars removed using proper motion, is plotted in the right panel. At the top of the main sequence, there is a bend (roughly $V = 17$ in the left panel) that indicates where stars have "turned off" from the main sequence - these stars have exhausted the hydrogen in their cores and are evolving towards the giant branch. This image is reproduced from Richer et al. (2013) [15].

1.1.3 Accretion Disk Emission

To understand the observed optical and X-ray emission from an accretion disk, a number of assumptions must be made about its structure. The primary approximation made to develop the disk dynamics is to assume that the flow of gas in the disk is limited to the plane of orbital motion, known as the *thin disk approximation* [3]. If changes to the accretion disk occur on timescales slower than the viscous timescale, then the disk will evolve in what is known as the *steady state* [3]. A complete discussion of the assumptions in the thin disk approximation can be found in Frank, King, and Raine (2002) [3]. However, a key element of this model is that the disk is optically thick in the vertical direction, perpendicular to the orbital plane. This means that each piece of the disk radiates like a blackbody, with inner portions of the disk radiating as a blackbody of higher effective temperatures. The total observed spectrum across the face of the disc is a combination of all these blackbodies, known as a multi-color blackbody. The emitted spectrum of the disk is represented by:

$$F_\nu = \frac{4\pi h \cos(i)\nu^3}{D^2} \int_{R_*}^{R_{out}} \frac{RdR}{e^{\frac{h\nu}{kT(R)}} - 1}. \tag{1.6}$$

Here, D refers to the distance to the source, $\cos(i)$ is the inclination of the source, h is the Planck constant. We choose R_{out} to be the outer edge of the accretion disk, and we set $R_\star$ to be the surface of the compact object (in the case of a NS or WD) or the last stable circular orbit (in the case of a BH). Additionally, the temperature of the disk T at a radius R is given by [3]:

$$T(R) = \left\{ \frac{3GM\dot{M}}{8\pi R^3 \sigma} \left[1 - \left(\frac{R_\star}{R} \right)^{\frac{1}{2}} \right] \right\}^{\frac{1}{4}}, \tag{1.7}$$

Here, $\dot{M}$ is the mass accretion rate, and $R_\star$ is the inner radius of the accretion disk. Note that for a neutron star, this assumption implies that the accretion disk extends to the surface. This is not always true in practice, especially in the presence of magnetic fields (see Section 1.1.4), but it is nonetheless a reasonable approximation for

the analysis presented here. The resultant spectrum for typical white dwarf parameters is given in Figure 1.4. Additionally, we will define a characteristic inner disk temperature, given by:

$$T_\star = \left(\frac{3GM\dot{M}}{8\pi R_\star^3 \sigma} \right)^{1/4}. \tag{1.8}$$

Several regions of the spectrum can be reasonably approximated by a power-law that has the form:

$$F_\nu \propto \nu^{\Gamma_\nu}. \tag{1.9}$$

Note that in *SYNPHOT* (discussed below in 3.1.3), power-laws are evaluated in wavelength-space rather than frequency-space. The index of a frequency space power-law Γ_ν is related to the index of a wavelength-space power-law Γ_λ by::

$$\Gamma_\lambda = -\Gamma_\nu - 2. \tag{1.10}$$

Several regions of this spectrum are of interest [3]:

1. For low frequencies, where $\nu \ll kT(R_{out})/h$, the spectrum has a Rayleigh-Jeans tail that resembles a power-law of index $\Gamma_\nu = 2$, $F_\nu \propto \nu^2$ ($\Gamma_\lambda = -4$).

2. For high frequencies, where $\nu \gg kT(R_\star)/h$, the spectrum has a Wien form, and declines exponentially.

3. For intermediate frequencies, $kT(R_{out})/h \ll \nu \ll kT_\star/h$, the spectrum resembles a power-law of index $\Gamma_\nu = \frac{1}{3}$, $F_\nu \propto \nu^{\frac{1}{3}}$ ($\Gamma_\lambda = -\frac{7}{3}$). This portion of the spectrum is known as the "flat" or "characteristic" disc spectrum.

In the X-ray regime, the spectrum can be easily modelled using the *diskbb* model (used in XSPEC, described in Section 2.1.2), a multi-colour disc blackbody (see Section 2.1.4). In the optical regime, it is expected that the portion of the emitted spectrum will be close to or inside the "flat" spectrum, motivating the choice of a

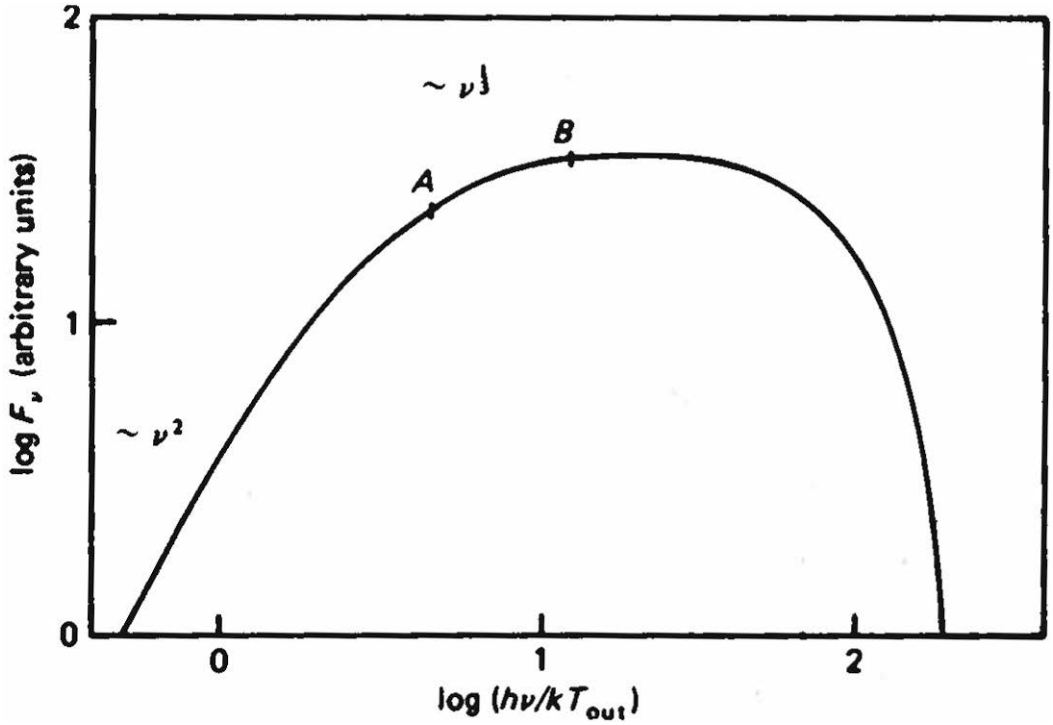

Figure 1.4: Accretion disk multi-color blackbody spectrum [3]. This model is for a white dwarf with the outer edge of the accretion disk $R_{out} = 250R_\star$. There are two regions of interest. The left side of the spectrum, marked with ν^2, indicates the Rayleigh-Jeans tail of the spectrum at low frequencies, where the spectrum can be approximated by a power-law of index $\Gamma_\nu = 2$. The region between points A and B shows the "flat" portion of the spectrum at intermediate frequencies, where the spectrum behaves as a power-law of index $\Gamma_\nu = 1/3$. For white dwarfs, this region is rather short, but for neutron star accretion disks, where $R_{out} \gg 250R_\star$, this region encompasses a larger range in $\frac{h\nu}{kT_{\rm out}}$.

power-law approximation, in Section 3.2.1. A justification of this choice of approximation is given in Section 4.1.

1.1.4 Propeller Effect

The simple prescription of a steady state, thin accretion disc is not always sufficient to describe binaries involving neutron stars, since accretion onto the surface of a compact object will only proceed in this prescription in the absence of strong magnetic fields. Neutron stars can possess strong magnetic fields, of order 10^{12} G,

causing the ionized accretion flow to be interrupted and reach the surface by being channeled to the magnetic poles. Thus, only a portion of the star is effectively accreting [3]. A simple schematic of this process is given in Figure 1.5. For material to be channelled on the magnetic poles, the Alfvén radius, a measure of the radius at which magnetic forces dominate the accretion flow, must extend beyond the surface of the compact object. The Alfvén radius is given by [3]:

$$r_M = 5.1 \times 10^8 \dot{M}_{16}^{-2/7} M_1^{-1/7} \mu_{30}^{4/7} cm, \tag{1.11}$$

where $\dot{M}_{16}$ is the accretion rate units of 10^{16} g s^{-1} and μ_{30} is the magnetic moment, measured in units of 10^{30} G cm^3. For a highly magnetized neutron star, accretion will not be efficient if the accreting NS is rotating too quickly. Inside the Alfvén radius, material is forced to rotate with the magnetic field. If the angular velocity of the accreting NS (and, consequently, its magnetic field) exceeds the Keplerian angular velocity of the infalling material from the disc at the Alfvén radius, the accreted material will then be accelerated by the B-field, pushing it outwards and inhibiting accretion [3]. Some material may accelerate quasi-periodically through Rayleigh-Taylor instabilities in the flow, but in general this *propeller effect* can cause accretion to be inefficient, generating an observed X-ray luminosity that is lower than what might be expected for a particular geometry [16, 17, 18]. For some sources, (discussed below in Section 1.2.1) the propeller effect is a potential explanation for their observed characteristics [19].

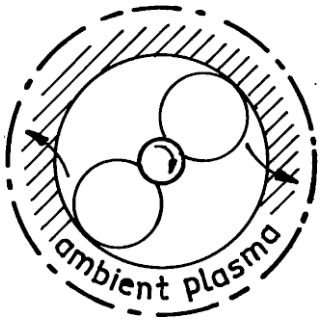

Figure 1.5: Conceptual illustration of the propeller effect [16]. The rapidly rotating neutron star (central circle) exerts strong pressure on the ambient plasma (the accretion disk, in this case, outer shaded portion) because its magnetic field repels inflowing matter (indicated by the arrows), causing inefficient accretion.

1.2 M15 X-3

1.2.1 Very Faint X-ray Transients and Accretion

Since the *Uhuru* era, observations conducted by progressively more sensitive X-ray telescopes, such as *Einstein*, *ROSAT*, and *Chandra* have probed fainter regimes of X-ray emission. For a more thorough discussion of *Chandra*, the X-ray telescope used in this work, see 2.1.1. One way in which transient X-ray sources can be broadly empirically categorized is by the peak of their X-ray luminosity during their active state, $L_{X,\mathrm{peak}}$. In this prescription, we discuss three classes of transient X-ray sources [20]:

1. Sources with $L_{X,\mathrm{peak}} = 10^{37-39}$ erg s^{-1} are known as the *bright* X-ray transients.

2. Sources with $L_{X,\mathrm{peak}} = 10^{36-37}$ erg s^{-1} are classified as *faint* X-ray transients.

3. Sources with $L_{X,\mathrm{peak}} = 10^{34-36}$ erg s^{-1} are known as the *very faint* X-ray transients (VFXTs).

Although the former two have been observed since the era of *BeppoSAX* (and earlier, in the case of the bright X-ray transients), the advent of *Chandra* has allowed

for the identification of the VFXT class [21]. VFXTs are fascinating from a binary evolution perspective, since most are believed to spend $< 10\%$ of their time in the "bright" state, implying an extremely low rate of mass transfer from the companion to the compact object, $\lesssim 10^{-13} M_{\odot}$ yr^{-1} [22] (note: 1 $M_{\odot}$ yr$^{-1} = 6.3 \times 10^{25}$ g s^{-1}). Low mass transfer rates may indicate extremely low mass companions, below about $0.01 M_{\odot}$ [22].

For conventional binary evolution, and a traditional mass accretion history, the above implies that these systems originally had higher-mass companions (of perhaps a solar mass) that have been reduced to $0.01 M_{\odot}$ by mass transfer to the compact object. This is problematic since the amount of time required for such evolution to take place generally exceeds the age of the Universe [22]. There are several alternative scenarios which are typically introduced to explain these low accretion rates. It is possible that some systems are being observed at an unfavourable inclination, but since the accretion disk can only meaningfully block X-ray emission at an inclination within about 15 degrees of edge-on, this is not a viable explanation for all VFXT systems [23]. Another option is to suggest that the low mass companion is primordial; that is, it has always been low-mass, implying a brown-dwarf or planetary companion [22]. If the companion is not primordially low-mass, then a high-mass accretor, which would be an intermediate-mass black hole (IMBH), may be needed to reduce the companion to the required low mass within the age of the Universe [22]. It has been argued by in't Zand et al. (2005) that for systems with $L_x < 10^{36}$ erg s^{-1}, the disk can only be kept ionized if it is very small, which implies an ultracompact system (through the short orbital period required) [24]. It is also possible that VFXT systems may be neutron star accretors experiencing inefficient accretion through a propeller effect (discussed in Section 1.1.4) [16, 17]. Since the majority of these scenarios rely on a companion with a relatively specific mass, the nature of VFXT systems can be constrained by observations of the companion at longer wavelengths, closer to the optical regime where the companion is expected to emit more strongly. It is important to note that VFXTs may not be a homogenous

group given some of these explanations could be true for certain sources while not being generally true for the entire VFXT population.

1.2.2 M15 X-3: Known Observational History

M15 X-3 is a VFXT located in the globular cluster M15 (NGC 7078) at a distance of D = 10.3 kpc [25]. This source, located 20" away from the core of M15, was first discovered from *Chandra* archival data in 2009, as outlined in [19]. Unlike most VFXTs, M15 X-3 is located in a globular cluster rather than in the direction of the Galactic Centre, meaning multi-wavelength observations of the source are practical due to low extinction. Here we summarize the key parameters determined from these observations.

From the *Chandra* and *ROSAT* observations available, taken from 1992 to 2007, this source was observed in two luminosity states.

1. In 1994, 1995, 2004 and 2007, M15 X-3 was observed at a luminosity of $4-8\times10^{33}$ erg/s.

2. In 2001, M15 X-3 was observed in quiescence at a luminosity of $\approx 2\times10^{31}$ erg/s (in 2000, it was also observed in quiescence though only at an upper limit).

Consecutive observations of M15 X-3 in the same year have found it to be in the same luminosity state, implying that M15 X-3 is likely persistently accreting in one state for a few years before switching states. Archival observations from the *Einstein* era (late 1970's) generally constrain its luminosity to $< 10^{35}$ erg s^{-1}. However, most observations with other instruments generally lack the spatial resolution to cleanly identify M15 X-3 because it is located only 20" away from two bright low-mass X-ray binaries, AC-211 and M15 X-2 (see Section 2.1.2), which contaminate the field. In general, these other observations only provide upper limits to the luminosity of M15 X-3.

Spectral analysis of M15 X-3 in its bright state showed that it was well-described by a relatively hard power-law of index $\gamma = 1.51 \pm 0.14$ (also see Section 2.1.4) [19]. In its faint state, M15 X-3 either was detected by instruments that have very poor spectral resolution ($\Delta E/E \approx 1$). Based on hardness ratios, M15 X-3 appeared to be a soft source (typical of NS LMXBs in quiescence). Obtaining a quiescent spectrum of M15 X-3 would require a very deep, time-constrained observation with *Chandra* ACIS (see Section 2.1.1).

Optical observations of M15 X-3 reported, discussed below, are extremely limited [19]. Although a potential optical counterpart has been detected, no instrument with angular resolution poorer than the *Hubble Space Telescope* (*HST*, fully described in section 3.1.1) is capable of separating the counterpart from other sources in this crowded field (although M15 X-3 lies outside of the core, this region of the cluster is sufficiently dense to make separating it from other stars in the field difficult - see Figure 3.2). Additionally, M15 X-3's position 20" from the core places it outside of most extensive observing campaigns with *HST*. Prior to this work, only three observations in two separate epochs detected the counterpart. In 1994, it was measured in the ultraviolet filter $F336W$ to have a magnitude of $U = 21.5 \pm 0.2$. In 2002, in the visible-light filter $F555W$ it was measured to have a magnitude of $V = 22.0 \pm 0.2$. Additionally, it was detected in 2002 in the blue filter $F438W$ at only $B = 23.7 \pm 0.8$, but with a large photometric error making the detection marginal at best. Comparing these measurements with other sources in M15 in the same observation showed evidence of excess emission in the ultraviolet compared with the main-sequence, which is a potential signature of an accretion disk in an X-ray binary.

With these combined observations, it is difficult to constrain the nature of M15 X-3's companion. Without clearer detection of the source in deeper *HST* observations, it is not possible to rule out the possibility of a brown-dwarf (or smaller) sized companion. In this work, we present the results of a near-simultaneous X-ray and optical observation of M15 X-3, to determine the most likely accretion scenario that explains the VFXT behaviour of M15 X-3.

Chapter 2

X-Ray Observations of M15 X-3

2.1 X-Ray Observations - Reduction and Extraction

2.1.1 The Chandra X-Ray Observatory

The *Chandra* X-Ray Observatory is a space-based telescope designed for high-resolution X-ray imaging, photometry, spectroscopy, and timing analysis over a range of soft X-rays from 0.3 - 10 keV. We used two of the four *Chandra* instruments in this analysis. The High Resolution Camera (HRC) provides the best spatial and timing resolutions of any *Chandra* instrument. It however does not have spectral information. The Advanced CCD Imaging Spectrometer (ACIS) provides the best energy resolution, but is susceptible to pileup (see Section 2.1.4). Additionally, the ACIS lacks a shutter, which means that for bright sources photons detected during the readout process will be assigned to the incorrect row, generating a long "readout streak" in the direction of event readout (see Figure 2.1).

When a given field containing X-ray sources is observed, an event file is generated that contains position, timing, and (if applicable) energy information for each photon incident on the detector. In principle, each event could be a photon or a cosmic ray. Cosmic rays are filtered during processing on the basis of the ASCA grade system, which will reject events based on energy (high-energy events, typi-

cally above 15 keV, are likely to be cosmic rays) and based on the shape of the event on detector pixels. Cosmic rays are filtered out during the automated processing that converts a level 1 events file to a level 2 events file. A complete discussion of the event grade process can be found in the *Chandra Proposer's Observatory Guide*. When processing *Chandra* data, one must consider the effective area (sensitivity of the CCD to different energies), detector response matrix (describes how energies of incoming photons are recorded), and aspect solution (time-dependent orientation of the telescope) during the data reduction process, described below.

2.1.2 X-Ray Data Reduction

We use two packages in the reduction and analysis of the *Chandra* data, the Chandra Interactive Analysis of Observations (CIAO) package and the High Energy Astrophysics software package (HEAsoft). CIAO provides tools for manipulation and extraction of the .FITS files directly produced by *Chandra* while HEAsoft provides the tools used for visualization (DS9) and spectral analysis (XSPEC). In this work, the software versions used were CIAO 4.6, CALDB (the calibration database for *Chandra*) version 4.5.9, and the August 2012 version of the time-dependent gain-files.

For ACIS-S and HRC-I observations, the first step is reprocessing the data products using the `chandra_repro` script to create a new level 2 events file, which is the .FITS file used for data analysis (after it has been cleaned for cosmic rays). Although each *Chandra* data set includes a level 2 events file, it is not guaranteed to have the latest calibration, so applying `chandra_repro` to datasets before analysis is standard practice to create consistent datasets.There are, in total, 4 ACIS and 5 HRC datasets available for analysis, shown in Table 2.1.

The most recent ACIS observation (ObsID = 13710) is a much shorter exposure (5 ks) than the other 3 ACIS observations (total exposure time 100 ks), but it is near-simultaneous with a *Hubble Space Telescope* (*HST*) observation taken the same week. This implies that if M15 X-3 is found to be in a consistent spectral state across

all four observations, the longer, non-simultaneous ACIS observations can also be used to infer the state of the system at the time of the *HST* observation.

ObsID	Date	Exposure [ks]	Instrument	L_x erg s^{-1}
1903	2001-07-13	9.1	HRC-I	$5^{+5}_{-3} \times 10^{31}$
2412	2001-08-03	8.82	HRC-I	$1^{+4} \times 10^{31}$*
2413	2001-08-22	10.79	HRC-I	$9^{+10}_{-7} \times 10^{31}$
9584	2007-09-05	2.15	HRC-I	$6^{+2}_{-2} \times 10^{33}$
11029	2009-08-26	34.18	ACIS-S	$8.3^{+0.4}_{-0.4} \times 10^{33}$
11886	2009-08-28	13.62	ACIS-S	$9.9^{+0.7}_{-0.7} \times 10^{33}$
11030	2009-09-23	49.22	ACIS-S	$9.2^{+0.4}_{-0.4} \times 10^{33}$
13420	2011-05-30	1.45	HRC-I	$5^{+2}_{-1} \times 10^{33}$
13710	2012-09-18	4.88	ACIS-S	$1.0^{+0.1}_{-0.1} \times 10^{34}$

Table 2.1: Summary of *Chandra* observations of M15 X-3. Observations marked with a * indicate observations for which only an upper limit is available.

For both the HRC and ACIS data sets, the next step is to identify the extraction regions containing the source and an appropriate region for estimating the local background. For M15 X-3, there are two complicating factors. The first factor is the presence of two bright LMXBs, AC-211 and M15 X-2, which lie only 20" away from M15 X-3 (bottom source), as seen in Figures 2.1 and refHRCimage. This means that background regions had to be carefully selected to avoid contamination from these bright sources. The second factor is that in the three 2001 HRC observations, M15 X-3 is not clearly visible since the source is in quiescence.

To obtain positions for M15 X-3 in these observations, we use the HRC datasets where it is clearly detected (ObsIDs 9584, 13420) and then shifted for the 2001 HRC observations based on the change in positions of the bright LMXBs between datasets where M15 X-3 is bright to datasets where it is faint. The size of the extraction and background regions in HRC observations was determined by applying photon raytracing centred on M15 X-3's position on the detector using ChaRT, a raytrace code that simulates a collection of photons passing through *Chandra*'s optics. The extraction region was chosen to be the region centred on M15 X-3 that contained

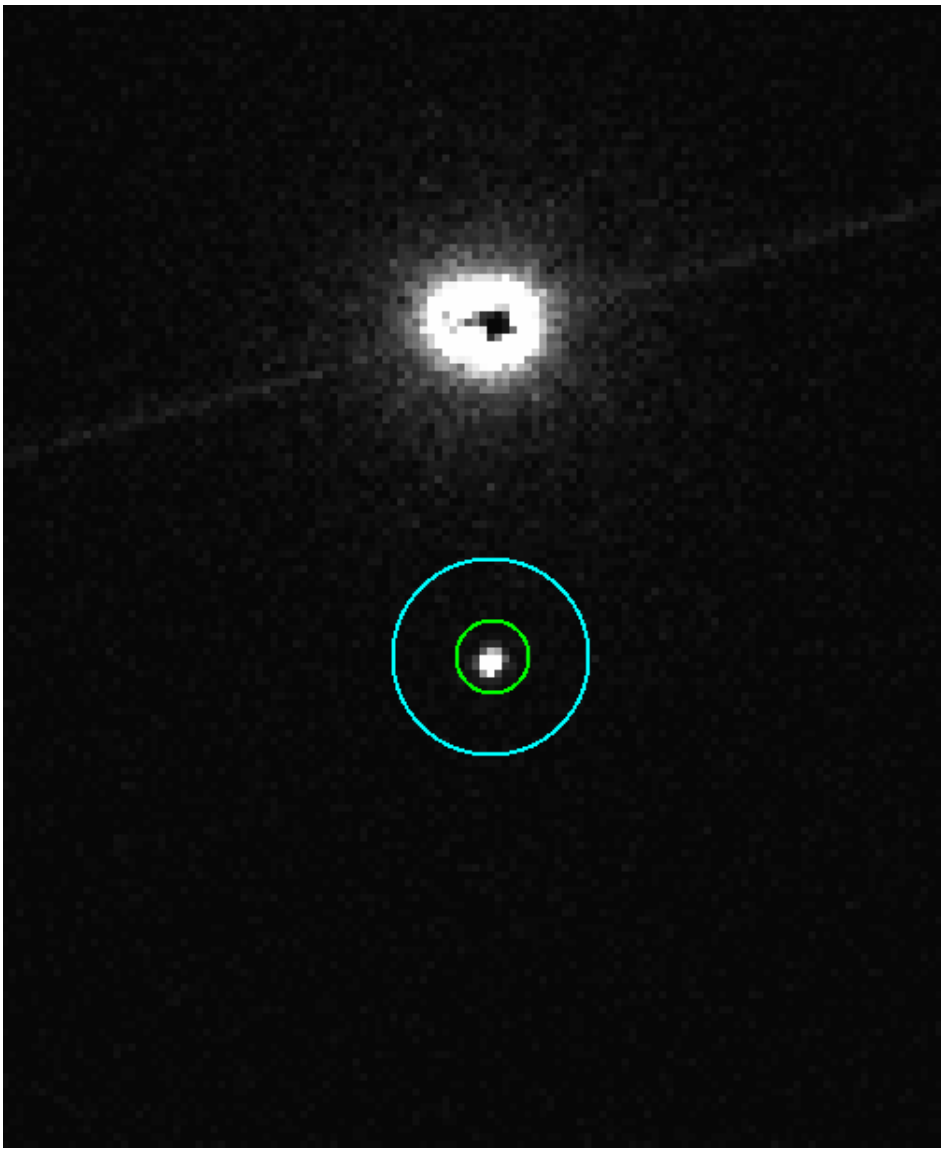

Figure 2.1: *Chandra* ACIS-S image of M15 (ObsID 11030). The interior green circle (size 2.4") indicates the region from which the spectra of M15 X-3 was extracted. The annulus formed by the inner circle and the outer (size 6") cyan circle indicates the region from which the background spectra (for background subtraction) is taken. Note that on this instrument, the two bright LMXBs AC-211 (slightly to the left) and M15 X-2 (slightly to the right) are difficult to distinguish. Two instrumental artifacts are visible in the image. The dark spot in the centre of the LMXBs (at approximately the location of M15 X-2) indicates that the very bright center of this image has been filtered due to pileup effects (see Section 2.1.4). In addition, the long line that lies on either side of the bright LMXBs shows the readout streak, as discussed in Section 2.1.1.

90% of the raytrace counts, while the background region was chosen to be a thin annulus extending beyond the region containing 99% of the raytrace counts that also excludes the 99% regions for the two other bright LMXBs. The resulting extraction and background regions resemble those in Figure 2.2. This procedure was used for all of the HRC observations, including ones where M15 X-3 was clearly detected, for consistency.

For the ACIS-S data, the clear detection of M15 X-3 in all observations makes source extraction much simpler. The source regions were all selected to be a 2.4" circular region centred on M15 X-3's position enclosed by a 6" radius annulus that was used as a representative background region. The resulting extraction and background regions are those depicted in Figure 2.1.

The next step in analyzing the HRC data is to perform photometry, which is discussed in Section 2.1.3. Since ACIS data contains the desired spectral information needed to characterize the M15 X-3 system, the next step in analyzing ACIS data is to extract a spectrum of the source, discussed in Section 2.1.4.

2.1.3 X-Ray Photometry (HRC)

For photometery with HRC, once regions have been generated, the count rates and fluxes are determined using the `srcflux` tool. This tool, when supplied with source and background regions, estimates the source count rate with Bayesian statistics using the `aprates` tool. Once the count rate was determined, the unabsorbed flux was estimated using PIMMS, a Chandra Proposal Toolkit, which gives fluxes consistent with those obtained from spectral fitting, as well as being consistent with [19]. For observations where M15 X-3 was not clearly detected, the PIMMS model was a blackbody of with $kT = 0.135$ keV. If M15 X-3 was in its bright state, the PIMMS model applied was a power-law with photon index $\Gamma = 1.4$ (see Section 2.1.4). In both cases, it is assumed that the equivalent hydrogen column density is $N_H = 4.6 \times 10^{20}\,\mathrm{cm}^{-2}$ (this procedure was adopted from [19]). The results of the HRC photometery are discussed in Section 2.2.2 and shown in Table 2.1.

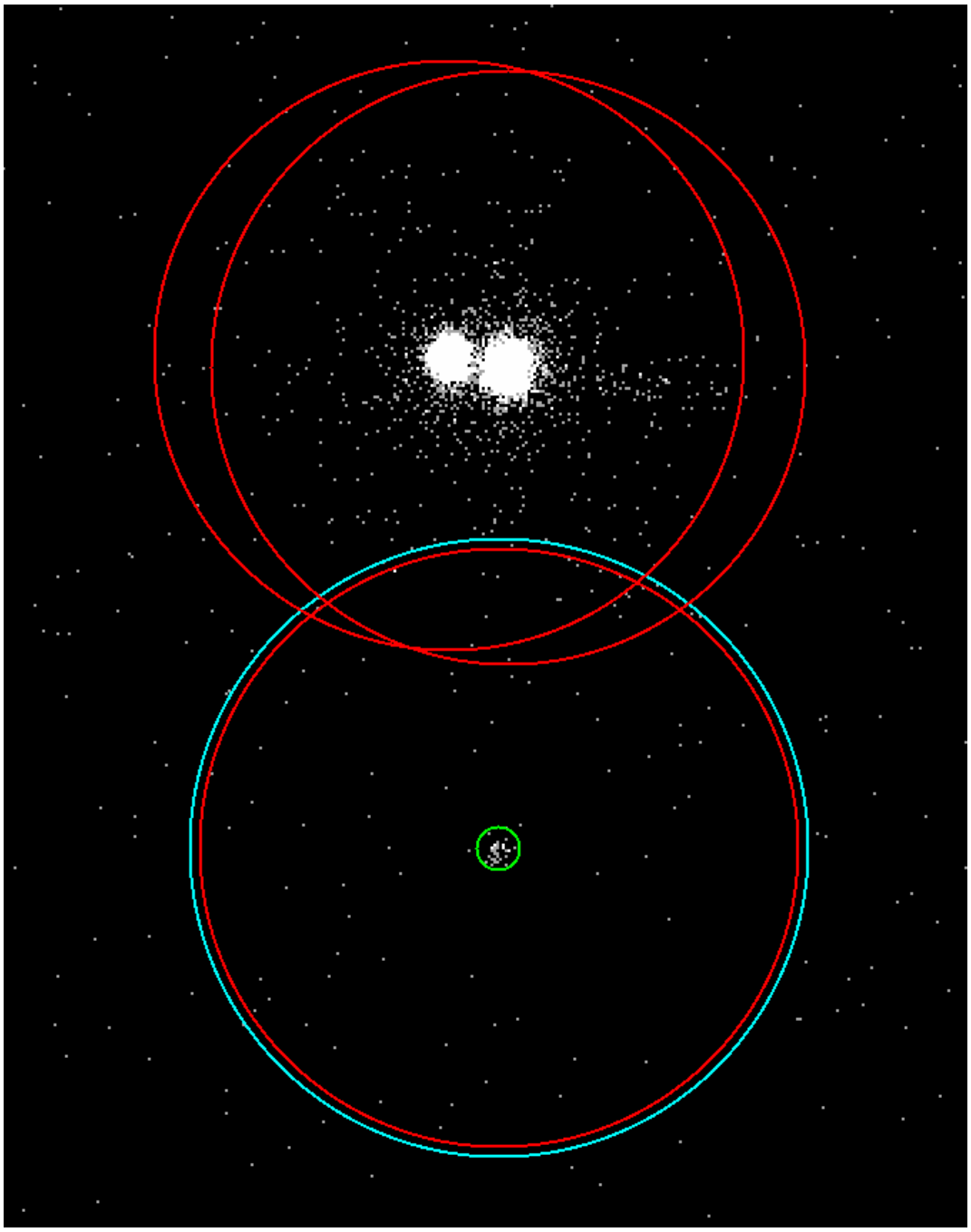

Figure 2.2: *Chandra* HRC-I image of M15. The small green circle indicates the extraction region for M15 X-3, the region that is expected to contain 90% of the counts from a ChaRT raytrace. The large red circles indicate the 99% count regions for AC-211 (top left source), M15 X-2 (top right source), and M15 X-3 (bottom source). The thin cyan region indicates the region from which the background was extracted, with the red regions excluded. The thin annulus formed by this region selection has an area roughly 5 times the size of the M15 X-3 extraction region.

2.1.4 Spectral Extraction and Fitting with XSPEC (ACIS)

Extraction of spectra from ACIS data is performed using the `specextract` script. This script is a combination of several CIAO tools. The `dmextract` command creates a PHA file, containing pulse heights which are mapped to photon energies by considering both the effective area (through `mkarf`) and the detector response (through `mkacisrmf`). A key choice when generating spectra is to consider the number of counts per energy bin. Too many counts per energy bin will wash out spectral information, whereas too few counts per bin will make statistical uncertainties too large for spectral fitting to be useful. A reasonable choice is to require a minimum of 25 counts per bin, which ensures that using Gaussian statistics for errors on physical quantities derived from fitting is relatively accurate. After the spectra are grouped using the `dmgroup` command to have a minimum of 25 counts per bin, they are suitable for spectral fitting with the X-ray spectral fitting package XSPEC 12.8.0.

XSPEC provides a powerful package for fitting spectra to a variety of useful physical and phenomenological models. To compare the model with data, the model is convolved with the instrument response to produce a predicted count rate in each bin. By default, XSPEC performs forward-fitting using a Levenberg-Marquardt algorithm, and determines its best fit using the χ^2 statistic. Since the χ^2 statistic assumes a Gaussian distribution of counts in each bin, this method is only valid if the number of counts per bin is not too small.

An additional consideration with XSPEC (and in analyzing CCD-based data in general) is the possibility for *pileup*. For sources that have a sufficiently high count rate, the odds that two (or more) photons will strike the same pixel within one frame time ($t_{frame} = 3.24014s$ for our observations taken with ACIS-S) is very large. When this occurs, the detector interprets the multiple photons as a single photon with an energy approximately equal to the sum of all the energies of the photons striking during the frame. Since photons with an energy above a certain threshold are rejected by the detector as being high-energy cosmic ray background, (either by the telescope

itself or during data grading) this can lead to an underestimate of the events detected from a bright source. In the case of very bright sources, it can lead to a "hole" in the image, as observed in Figure 2.1. Although M15 X-3 is faint enough that there are no clear holes in the source, the ACIS detector is sufficiently sensitive that M15 X-3 is stillaffected by pileup. To account for pileup, all spectral models used in the analysis are convolved with a “pileup" model, which applies a correction in cases where the effect is not too strong.

The simplest model used is the power-law, listed in XSPEC as `pegpwr`. It is a simple phenomenological model of the form:

$$C(E) = AE^{-\Gamma}. \tag{2.1}$$

The quantity Γ is referred to as the photon index. Many physical models within the X-ray region can be approximated by a power-law. It is possible that this emission could be from the hot corona surrounding the NS, a shock in a pulsar wind, or other non-thermal accretion-related effects that are difficult to model.

The other phenomenological model used is a broken power-law (`bknpow`), which is a model where the spectrum is a power-law of index Γ_1 up to a break-energy E_{break}, where it becomes a power-law of index Γ_2. This is useful for modelling spectra that show evidence of non-thermal curvature.

Multiple XSPEC thermal models were also used during the fitting process. The simplest is `bbodyrad`, which models a blackbody of temperature kT with a normalization related to the surface area of the emitter (normalization $= R^2_{\text{emitter}}/D^2_{source}$, the square of the source radius in km over the distance to the source in units of 10 kpc). Blackbody models are generically useful but in the case of a source that is believed to be a NS accretor, they could be used for the entire NS surface, NS surface hotspots or an accretion disk. The thermal spectrum of the accretion disk is generally best described by the multi-temperature disk blackbody `diskbb`, which models a disk with inner radius temperature kT and a normalization related to the apparent

inner disk radius, distance to the source, and inclination. The other thermal model used in the analysis of M15 X-3 is the neutron star atmosphere model, `NSATMOS`. This model provides a spectrum interpolated from a grid of NS atmospheres for a given effective temperature $\log(T_{eff})$, mass M_{ns}, radius, R_{ns}, and distance [26]. Since prior evidence suggests that M15 X-3 is a weakly accreting NS with a low-mass companion, these models are all acceptable for testing against M15 X-3's spectra [19].

2.2 X-Ray Results and Analysis

2.2.1 X-ray Spectral Results

Previous spectral fitting of M15 X-3 in the 2004 HETGS observation found that the spectrum is well-described by an absorbed power law with photon index $\Gamma = 1.51 \pm 0.14$ [19]. In this analysis, all four available *Chandra* ACIS-S observations were fit simultaneously (see 2.1). For VFXTs that have spectral information available, they are often described with either a hard power-law, or a hard power-law with an additional softer thermal component [27]. This motivated the initial choice of a fit with a single absorbed power law (with the column density fixed at $N_H = 4.6 \times 10^{20}\,\mathrm{cm}^{-2}$ [28]) although a variety of fits were explored. Fitting with a single power law gives a reasonable representation for each observation ($\chi^2 = 214.13$ for 191 degrees of freedom (d.o.f), null hypothesis probability (nhp) = 0.12), which suggests that M15 X-3 is in a similar state with an X-ray luminosity of $\mathrm{L}_x \approx 0.8 \times 10^{34}$ ergs/s. This motivated the choice to jointly fit all four observations. In general, XSPEC permits model parameters to be either free (allowed to vary during the fitting process) or frozen (fixed and not allowed to vary during the fitting process). Additionally, when fitting multiple observations with the same model, one can also tie parameters together between multiple observations. In this case, the power-law index was tied across all four observations while we individually fit the power-law normalizations, which dictate the relative luminosities, for

each observation. This procedure provided an acceptable fit with a power-law of index 1.40 ± 0.03. A plot of the fitted spectrum for all four observations is given in Figure 2.3. We do not see a statistically significant improvement ($\Delta\chi^2 = -2.4$ for 3 fewer d.o.f.) when individually fitting power-law indices for each observation.. This provides further evidence that M15 X-3 is in the same spectral state across all four observations. The dependence of the fit on the column density N_H and the pileup grade parameter α (a quantity which describes the extent of pileup) was also tested, but fitting for these parameters did not significantly improve the result. This suggests that it is unlikely much additional intrinsic absorption occurs in M15 X-3 and that the pileup of the events is weak, respectively.

One unusual property of the fit obtained from a single power-law is the evidence of curvature in the residuals. Examining the residuals between 1-3 keV (Figure 2.3) shows a large number lie above the model. Alternatively, this can also be described as the residuals at high and low energies trending below the model. Regardless, this curvature suggests an alternate fit was necessary. Other VFXTs have shown evidence of a power-law component with an additional thermal component. Therefore, a combined spectrum of a power law + thermal component (`NSATMOS`, `bbodyrad`, and `diskbb`) was tested.

Adding an `NSATMOS` component (for the thermal component) does not improve the fit ($\chi^2/dof = 241.12/190$) and gives a neutron star surface temperature of $kT_{eff} \approx 8.6 \times 10^{-3}$ keV. This is the lower bound for the temperature parameter, and has a 1σ upper limit of 5.3×10^{-2} keV. At the upper bound, this component contributes $< 0.16\%$ of the 0.5-10 keV unabsorbed flux of the source, leading to the conclusion that M15 X-3's spectrum lacks an `NSATMOS` component.

Testing, instead, with a blackbody component, `bbodyrad`, does improve the fit ($\chi^2/dof = 187.90/189$) versus the single power law, although it creates problematic a physical interpretation. The blackbody component has an inferred temperature of $kT = 0.65$ keV over an emitting area of radius $R \approx 0.2$km. The interpretation of this result would be to assume that M15 X-3 contains a hot spot on the neutron

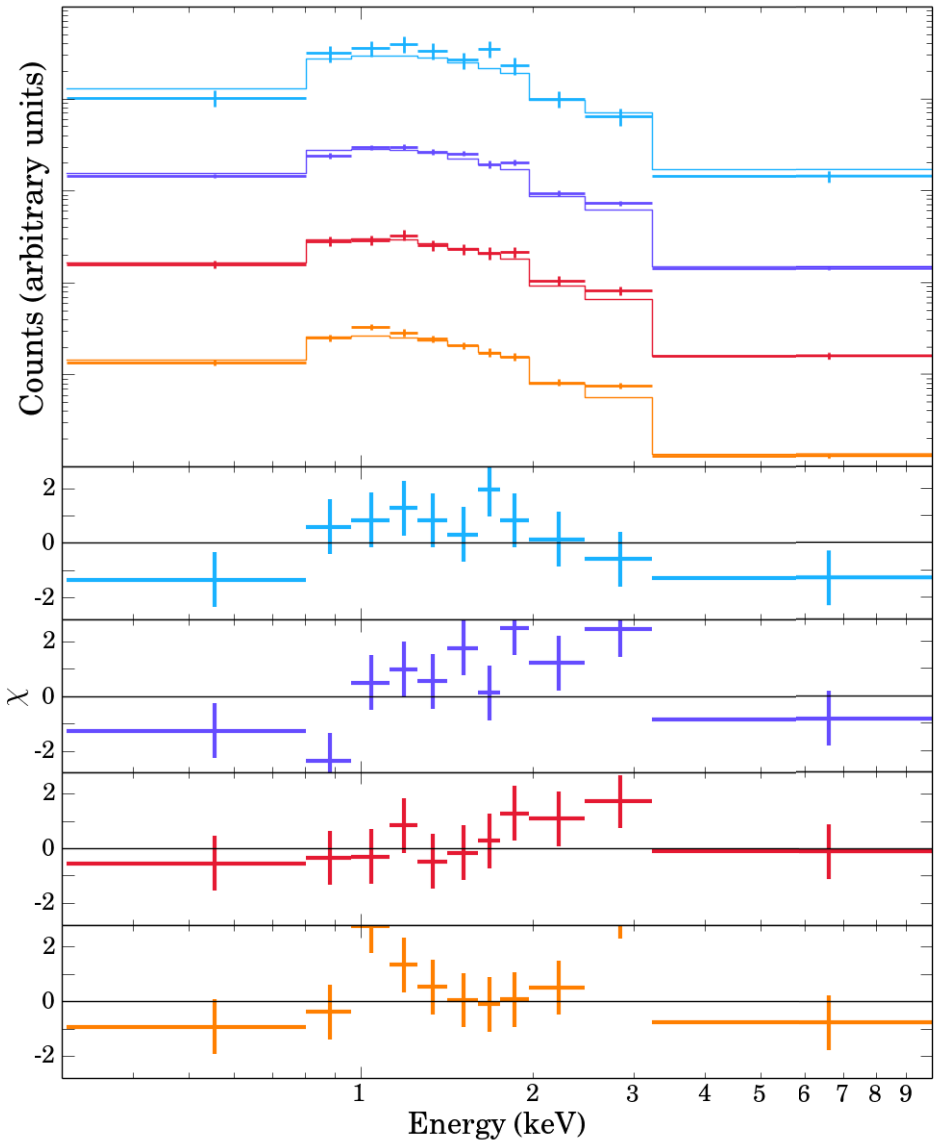

Figure 2.3: X-ray spectrum for M15 X-3, with the fit to a single power-law model. The observations are sorted by date with the most recent at the top (from top: ObsIDs 13710,11030,11886,11029). The bottom panels indicate the residuals to the single power-law fit. Note that many of the data points lie above the model between 1-3 keV and below the model outside this range. This data has been rebinned for plotting purposes.

star surface. However, given that M15 X-3 is a tremendously weak (≈ 2 orders of magnitude fainter) X-ray source compared with the general LMXB population ($L_{\rm X,peak} \lesssim 10^{34}$ erg s^{-1}, which implies weak accretion onto the NS surface itself), it is difficult to conceive of a reason why M15 X-3 might have such a hot spot.

Using the accretion disk blackbody model, `diskbb`, gives a similar improvement to the fit statistics that `bbodyrad` does ($\chi^2/dof = 187.90/189$), but also leads to problematic physical results. The physical parameters derived from the `diskbb` component gives a blackbody temperature of 1.2 keV with an inner disk radius parameter of $R_{\rm inner}\cos\theta = 0.06$km. For a face-on disk, such a result is aphysical, as it is smaller than the size of the neutron star itself. This requires that the inclination of the disk θ to be sufficiently large such that the inner disk radius is physical. However, in this scenario the disk would need to be nearly edge-on. Since M15 X-3 has shown no evidence of eclipsing, strong radio emission, or any evidence that suggests it is a much more powerful emitter being obscured by its disk, this scenario seems highly unlikely (see Section 4.3 for further discussion).

The presence of curvature in the fit residuals also motivated the choice to empirically use a broken power-law model, described above and modelled in XSPEC using `bknpow`. The resultant spectrum is shown in Figure 2.4. When M15 X-3's spectra are fitted with a broken power-law, the fit ($\chi^2/d.o.f. = 185.51/189$) is substantially improved over the single power-law or a single power-law + thermal model. A summary of the fit statistics and fit parameters for both the single power-law and broken power-law are given in Table 2.2. The fitted parameters describe M15 X-3's spectrum as a power-law of index $\Gamma_1 = 1.25^{+0.02}_{-0.01}$ up to an energy of $2.71^{+0.38}_{-0.05}$ keV, where it becomes a power-law of index $\Gamma_2 = 1.82^{+0.20}_{-0.02}$. To compare against the single power-law, an F-test gives a probability of 1.24×10^{-6}. This suggests that the broken power-law is a statistically superior description of M15 X-3's spectra. Initially this fit was achieved with the power-law indices and break energy tied across observations. Fitting with these parameters untied does not statistically improve the fit. This indicates there is no reason to suspect that these parameters

might be changing between observations. In addition, allowing the pileup parameter α or the column density N_H to vary does not improve the fit, which implies (as with the single power-law) that M15 X-3 is not piled up in these observations and does not have significantly higher intrinsic absorption than the cluster value.

If M15 X-3 is indeed a NS accretor, it is reasonable to ask whether there is any soft thermal component that can be separated from the broken power-law. Adding a thermal component does not improve the fit. We find $\Delta\chi^2 < 0.01$ for a change of 1 d.o.f. for the NSATMOS model, $\Delta\chi^2 = 0.01$ for a change of 2 d.o.f. for the addition of the BBODYRAD model, and $\Delta\chi^2 = 0.45$ for a change of 2 d.o.f. the addition of the DISKBB model. The broken-power law description of M15 X-3 is somewhat unusual, and seems to be unique in the literature amongst known VFXTs (see Section 4.4).

Parameter	Units	Single power-law fit	Double power-law fit
N_H	$10^{20}\,\mathrm{cm}^{-2}$	[4.6]	[4.6]
Γ_1		$1.42^{+0.03}_{-0.03}$	$1.28^{+0.06}_{-0.06}$
Γ_2		no data	$1.9^{+0.2}_{-0.2}$
E_{break}	[keV]	no data	$2.7^{+0.3}_{-0.6}$
L_X	MJD = 55069 10^{34} erg s^{-1}	$0.83^{+0.04}_{-0.04}$	$0.75^{+0.03}_{-0.03}$
	MJD = 55071 10^{34} erg s^{-1}	$0.99^{+0.07}_{-0.07}$	$0.89^{+0.06}_{-0.06}$
	MJD = 55097 10^{34} erg s^{-1}	$0.92^{+0.04}_{-0.04}$	$0.83^{+0.04}_{-0.03}$
	MJD = 56188 10^{34} erg s^{-1}	$1.0^{+0.1}_{-0.1}$	$1.0^{+0.1}_{-0.1}$
$\chi^2/d.o.f$		214.13/191	185.51/189
n.h.p.		0.12	0.56

Table 2.2: Summary of XSPEC fits of M15 X-3's combined spectra to single and broken power-law models. Values in square brackets are fixed at the cluster value. Errors on parameters are given at the 90% confidence level.

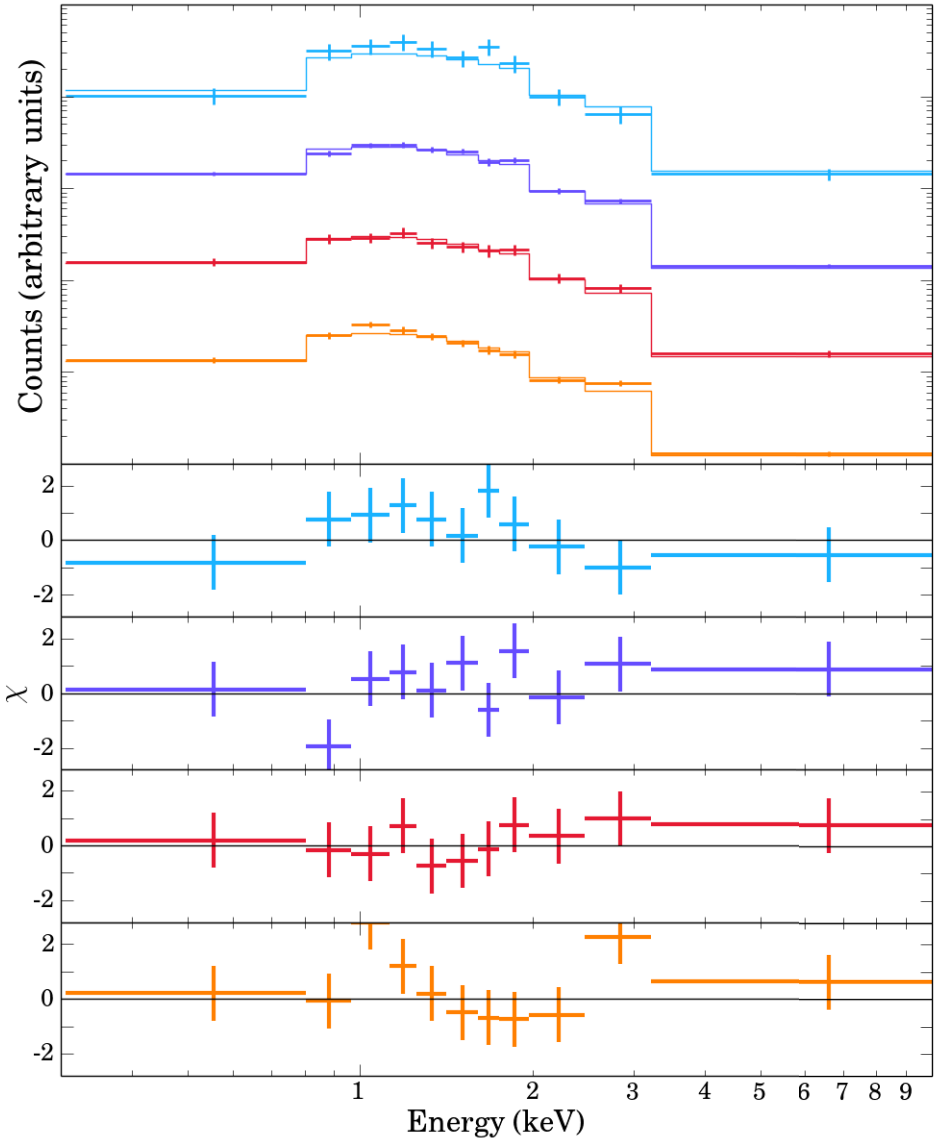

Figure 2.4: X-ray spectrum for M15 X-3 fitted to a broken power-law model. As with Figure 2.3, observations are sorted by date with the most recent at the top (from top: ObsIDs 13710,11030,11886,11029) and the data has been rebinned for plotting purposes.

2.2.2 Long Term X-ray Light Curve

The four ACIS and five HRC observations provide roughly a decade of coverage of M15 X-3's activity during the *Chandra* era. Adding the *Chandra* HETG observations and the observations taken with *ROSAT* in the pre-*Chandra* era can constrain M15 X-3's flux history over roughly two decades. All observations of M15 X-3 since the first *HST* observation of M15 X-3's optical counterpart are shown in Figure 2.5. Obtaining a thorough picture of M15 X-3's activity permits one to infer estimates of the duty cycle, and hence the time-averaged accretion rate. Broadly, VFXTs appear to belong to two classes. The majority in the literature describes short duty cycles ($< 10\%$) with outbursts of $L_X \approx 10^{34-36}$ erg s^{-1}, spending the rest of their time in quiescence [29, 30, 31, 20]. However, a small number of VFXTs persistently accrete at $L_X \approx 10^{34}$ erg s^{-1} with a relatively large duty cycle (50%) [24, 32, 27]. M15 X-3's long-term behaviour displays a very large duty cycle with a "bright" state luminosity of $6-10\times10^{33}$ erg s^{-1}. The time-averaged accretion rate and duty cycle are estimated using the results plotted in Figure 2.5 in Section 4.4.

2.2.3 X-ray Conclusions

Before considering the optical data obtained during the most recent ACIS observation, several important conclusions may be made about the X-ray behaviour of M15 X-3:

1. M15 X-3's spectrum in its bright state shows evidence of unusual curvature, which can be best empirically described with a power-law of index $\Gamma_1 = 1.25^{+0.02}_{-0.01}$ to the break energy $E_{\rm break} = 2.71^{+0.38}_{-0.05}$ keV, after which it becomes a power law of index $\Gamma_2 = 1.82^{+0.20}_{-0.02}$. In this bright state, M15 X-3 has a luminosity of $6-10\times10^{34}$ erg s^{-1}.

2. M15 X-3's spectrum seems to lack any kind of a statistically significant thermal component.

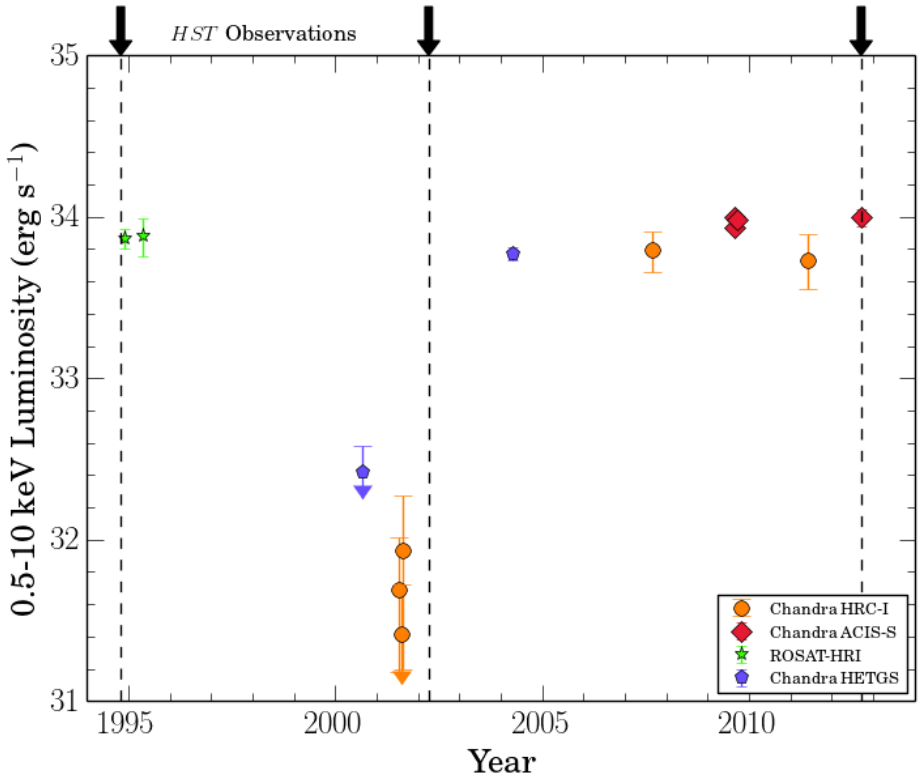

Figure 2.5: Long term light curve for M15 X-3. ROSAT and *Chandra* HETGS data are taken from [19], while the HRC-I and ACIS-S data was analyzed in this paper. The vertical dashed lines indicate HST observing epochs, including the 2012 observation that is nearly simultaneous with an ACIS-S observation.

3. M15 X-3's duty cycle is quite high, exceeding 50% with at least two observed state transitions - once from the bright state to quiescence between 1995 and 2001, and returning to the bright state between 2001 and 2005. This permits the time-averaged accretion rate to be inferred (see Section 4.4).

4. When considering the simultaneous *HST* observations, it can be assumed that M15 X-3 is emitting $\approx 10^{34}$ erg s^{-1} of X-rays - which is potentially important if the companion is being irradiated by the primary.

Chapter 3

Optical Observation of M15 X-3: Reduction, Results, and Analysis

3.1 Optical Observations - Reduction and Extraction

3.1.1 The Hubble Space Telescope

The *Hubble Space Telescope* (hereafter *Hubble* or *HST*) is a powerful space-based telescope that has provided imaging and spectroscopy between the near-ultraviolet and near-infrared wavelengths for over 20 years. In this research, data from the Wide Field Camera 3 (WFC3), which provides the largest field of view and best resolution of any *HST* instrument, was utilized. WFC3 replaced its predecessor, the Wide Field Planetary Camera 2 (WFPC2), during the last servicing mission in 2009. Aside from the WFC3 data primarily considered in this research, other usable data of M15 X-3 was taken with WFPC2. Data collected with these detectors is suitable for photometry in a variety of passbands. The general method by which CCD-based photometers like WFC3 collect data is to pass incoming photons through a filter (or passband) and then collect the photons with a photosensitive chip. The set of filters used (so that observations can be collected at different specific wavelength ranges) forms the photometric system of the telescope. WFC3 has two channels, each with

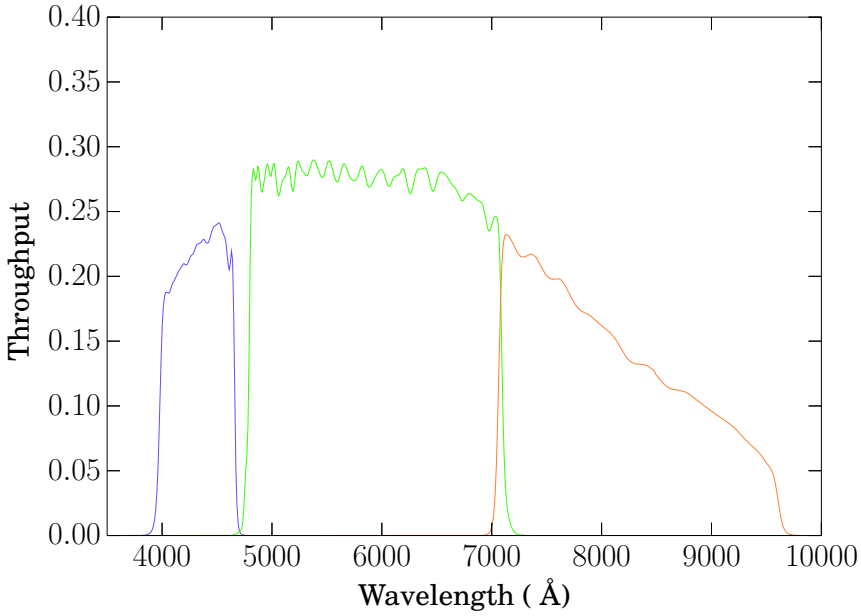

Figure 3.1: Plot of the *HST* throughputs for the filters used in this research. The left (blue) curve is the throughput for F438W, the *B* filter. The middle (green) curve plots F606W, the *V* filter. F814W, the *I* filter, is plotted by the right (orange) curve. Since these filters on the WFC3 are similar to the equivalent ones on its predecessor, WFPC2, the filters are referred to as the WFPC2 *B*, *V*, and *I* in the WFC3 Instrument Handbook.

a different set of filters. The ultraviolet and visible light (UVIS) channel contains a variety of wide and narrow-band filters, as well as legacy filters to overlap with previous instruments. The infrared (IR) channel contains a handful of useful wide-band and spectral line filters. Each filter can be characterized by the throughput, which is the sensitivity of the filter at individual wavelengths across its wavelength range. As an example, the throughput of the WFC3 filters used in this research are shown in Figure 3.1. Filters are identified in the Hubble system by their central wavelength and the approximate width (in wavelength space) of the bandpass. For example, the *B* filter used in this analysis is F438W, indicating it is a wide filter centred on 438 nm.

3.1.2 HST Photometry and Source Extraction

Similar to analysis of *Chandra* data, *HST* data requires some pre-processing before it is suitable for analysis. In this work, I only analyzed the observed magnitudes after they had been extracted. Therefore, the reduction steps to obtain the observed magnitudes are only described briefly here. The `Multidrizzle` software package is used to prepare the data in two ways. First, similar in goal to the event grading performed by *Chandra* analysis tools, `Multidrizzle` filters cosmic rays striking the detector by median filtering across multiple exposures. That is, if a cosmic ray strikes one location in one exposure, it is extremely unlikely that a second cosmic ray will strike the same location in a different exposure. Typical *HST* observations aim each exposure at a slightly different position on the sky. Multidrizzle combines the dithered observations (in sky coordinates) and corrects for geometric distortion due to telescope optics. Dithering helps smooth the effects of pixel-to-pixel variation (since each part of the sky will be sampled by different pixels in different exposures), can remove small detector defects, and (most importantly) improves image quality by providing some correction for undersampling by large pixels [33]. Following this processing, the data is ready for photometry to be performed using the `DAOPHOT` stellar photometry package. This package is designed specifically for performing photometry on crowded fields by identifying candidate stars and their aperture photometry profile. Applying knowledge of the point-spread function, it fits the position of the star and subtracts the corresponding profile of a point source at that position. This allows extraction of information about stars in regions where the light from multiple stars overlap. M15 is an extremely dense globular cluster that is core-collapsed, especially within the central arcsecond, making the field extremely crowded (core-collapsed clusters have luminosity profiles that increase all the way to the centre of the core, rather than flattening). Once photometry has been performed on the field, the magnitudes of individual stars may be extracted, as was done for M15 X-3's optical counterpart.

For this work, one orbit of *HST* was used, observing M15 in 3 filters (Principal

Investigator: C. Heinke, University of Alberta). The filters used were F438W (broad *B*), F606W (broad *V*), and F814 (broad *I*). Four dithered exposures in each filter were taken in the UVIS2 subarray mode (UVIS2-C1K1C-SUB), where we combined each set for a given filter using `Multidrizzle`. These observations were taken roughly one day before *Chandra* observation 13710 (see Table 2.1), making them nearly simultaneous (that is, within one day). A full summary of the *HST* observations taken for this work and in previous epochs is shown in Table 3.1.

Proposal ID	Date	MJD	Exposures (s)	Instrument	Magnitude
5742	1994-10-26	49651	3 x 600 F336W	WFPC2	21.5 ± 0.2
9039	2002-04-05	52369	12 x 16 F555W	WFPC2	22.0 ± 0.2
9039	2002-04-05	52369	4 x 40 F439W	WFPC2	23.7 ± 0.8
12751	2012-09-17	56187	4 x 83 F814W	WFC3	21.69 ± 0.04
12751	2012-09-17	56187	4 x 47 F606W	WFC3	22.34 ± 0.09
12751	2012-09-17	56187	4 x 340 F438W	WFC3	22.77 ± 0.12

Table 3.1: Summary of *HST* Observations of M15 X-3. Exposures are given as (number of exposures) x (exposure length in seconds). For example, the 1994 observation consists of 3 exposures of 600 seconds each in the F336W (ultraviolet or *U*) filter. Observations from previous epochs are taken from [19].

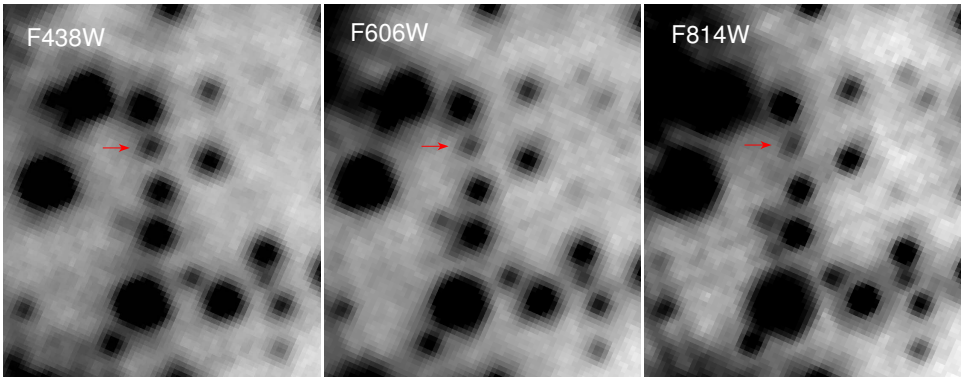

Figure 3.2: Finding charts for the optical counterpart of M15 X-3 as detected by *HST*. In each frame, the location of M15 X-3 is identified with a red arrow. These observations are simultaneous with *Chandra* ObsID 13710. Note both the crowding of the field (nearby stars) and the relative faintness of M15 X-3 compared to other sources in the field. These elements make it challenging to detect M15 X-3's counterpart with any telescope with resolution poorer than that of *HST*.

3.1.3 Simulating observations with SYNPHOT

The primary tool for analyzing the *HST* magnitudes obtained for this research is the synthetic photometry package `SYNPHOT`. `SYNPHOT`, developed by the Space Telescope Science Institute for use with *HST*, permits manipulations involving the *HST* bandpasses, with support for other photometric systems. In addition to analytical physical models, `SYNPHOT` supports multiple gridded libraries of stellar atmospheres and atlases of stellar spectra. `SYNPHOT` simulates HST observations by the following procedure:

1. The user selects the *HST* instrument filter/bandpass used for the observation.
2. The user selects the object (star from an atlas, atmosphere from a gridded model, simple physical model, or a mathematical combination of all of these) and calculates its spectrum from `SYNPHOT`'s library.
3. `SYNPHOT` convolves the spectrum (singular) with the passband to generate an observed spectrum.
4. `SYNPHOT` outputs the observation in the format and magnitude system chosen by the user. This could be plotting an observed spectrum (for a spectrometer) or determining count rates (for a photometer).

The tools of `SYNPHOT` make it useful for planning proposals by estimating the expected results from observing campaigns, as well as modelling existing data. In this work we use the predicted magnitudes generated by `SYNPHOT` to determine the most plausible model for M15 X-3's optical emission. For this sort of analysis, `SYNPHOT` is may be used in its python implementation, `PYSYNPHOT`.

3.1.4 Magnitude fitting with PYSYNPHOT

The primary goal in collecting the *HST* magnitudes of M15 X-3 is to determine the nature of the of low-mass companion of the system through fitting its optical/UV

spectral energy distribution. PYSYNPHOT provides a framework by which a grid in the fitting parameter space can be computed. The comparison between observed and expected (modelled) magnitudes is computed with a simple χ^2 goodness of fit analysis. Since magnitudes are actually logarithms of flux ratios, it is sensible to convert each magnitude to a flux before fitting because the magnitude errors are not small. The magnitude of an object m is related to the flux of an object F_i in a given filter i by:

$$\frac{F_{i,\text{object}}}{F_{i,\text{ref}}} = 10^{\frac{m_{\text{object}} - m_{\text{ref}}}{-2.5}}. \tag{3.1}$$

In this case, ref indicates a reference object. For these observations, the magnitudes were calibrated to vegamags, where the star Vega has a magnitude of 0 in all filters and all fluxes are proportional to Vega. Once the conversion to flux is made for each fit, the χ^2 statistic is defined by summing over the measurements from each of the 3 filters:

$$\chi^2 = \sum_{i=1}^{3} \frac{(F_{i,\text{observed}} - F_{i,\text{expected}})^2}{\sigma_i^2}. \tag{3.2}$$

The goodness of fit is determined by combining the χ^2 with the d.o.f., which, in this case, is equal to the number of data points minus the number of parameters fit in the model.

3.2 Optical Results and Analysis

3.2.1 Optical Fitting Results

Two principal results are generated by performing photometry on the M15 field. The first is a color-magnitude diagram (CMD) of the entire cluster, where comparing the position of M15 X-3's optical counterpart to the rest of the cluster provides indications of the source of M15 X-3's optical emission. As seen in Figure 3.3,

M15 X-3's optical counterpart is bluer (lies to the left of) than the main sequence for the cluster. Indeed, as one moves to bluer filters (from $B-V$ to $V-I$), M15 X-3 appears to move further to the left. The clear excess in bluer filters would suggest two possibilities for M15 X-3's optical counterpart:

1. M15 X-3's optical emission consists of a low-mass main-sequence companion and an accretion disk.

2. M15 X-3 (or at least its optical counterpart) is not a member of the cluster.

There are several reasons discussed in Section 4.2 why the latter possibility is unlikely. This analysis is conducted with the assumption that M15 X-3 is a cluster member.

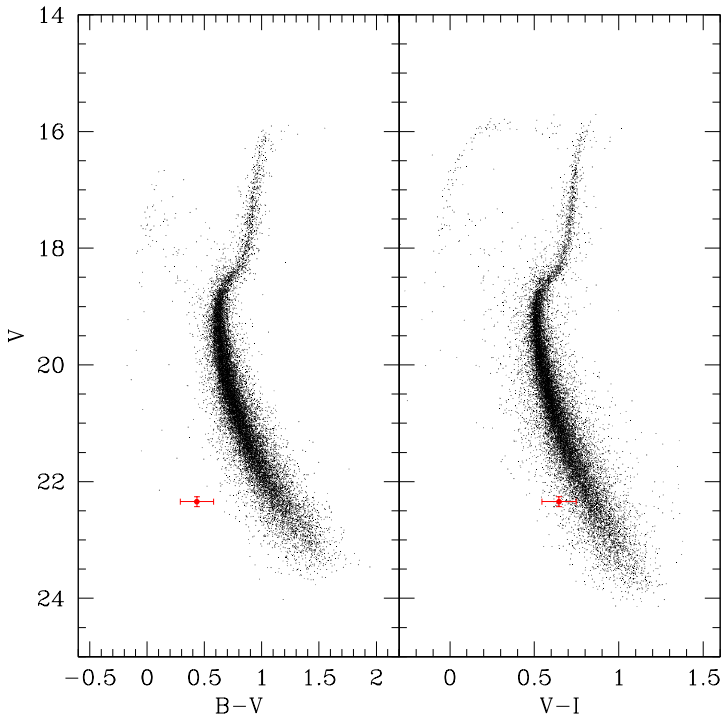

Figure 3.3: Color-magnitude diagrams for M15. Two colors are presented here: $(B-V)$ and $(V-I)$. The long black band of points represents the "main sequence" of M15. The bend in the main-sequence track at $V \approx 18.5$ indicates the turnoff point of the main sequence. The red point indicates the location of the optical counterpart for M15 X-3, with errors calculated based on the half-width of the main sequence. Note that M15 X-3 appears to be bluer than the main sequence, especially as one moves to bluer filters. Aside from M15 X-3's optical counterpart, only stars with small formal photometric error (< 0.025 mag) were kept to clean the image.

In making the CMD, the magnitudes for individual objects in the observation, in particular the optical counterpart for M15 X-3 (see Table 3.1), were also obtained. The 2012 observation of M15 X-3 yields a clear detection of the optical counterpart of the source in all 3 filters, as can be seen in the finding chart in Figure 3.2. To fit the 3 measured magnitudes, assumptions need to be made about the nature of the system. M15 X-3's position on the CMD in the most recent *HST* observation shows it to be bluer than M15's main sequence, which suggests optical emission due to the presence of both a low-mass main sequence companion and an accretion disk.

Motivated by the position on the CMD, M15 X-3's spectrum was chosen to be the sum of two components:

1. An optically thick accretion disk, approximated in the optical region by a power-law (see 1.1.3) with $\Gamma_\lambda = -\frac{7}{3}$ when held fixed, the conventional disk value [3].

2. A low-mass companion, assumed to be a main sequence star for M15's metallicity of $[M/H] = -2.0$ [34] (the abundance of elements other than hydrogen and helium, generally quoted compared to solar values), which indicates the population is metal-poor compared to the Sun.

For the low-mass companion, the Castelli-Kurucz atlas of stellar atmospheres (ATLAS9) is suitable since it contains reasonably low-mass stars similar to those expected for M15 X-3's companion given its relative dimness. This set of models uses the effective temperature $\log(T_{eff})$, gravity $\log(g)$, and metallicity $[M/H]$ [35]. To correlate these parameters to the companion mass, models of low-mass stars at metallicity $[M/H] = -2.0$ for particular masses from [34] are used. A mass range between 0.083 $M_\odot$ and 0.8 $M_\odot$is considered with linear interpolation of parameters applied where necessary to produce a well-spaced grid of masses. `SYNPHOT` also performs interpolation between models using a gridded table.

When fitting, the mass of the companion was always permitted to vary. The power-law index was first permitted to vary between -4 (corresponding to the Rayleigh-Jeans tail of the accretion disk, suitable for long wavelengths as discussed in Section 1.1.3) and -2 (which would occur at sufficiently short wavelengths that we would expect to be past the regime where the accretion disk is visible in optical bands). Instead of being a gridded parameter, the normalization of the power-law was solved exactly (after the other parameters were determined) by minimizing the χ^2 with respect to the normalization by assuming the flux F_i in a given filter i is described in the following way with a normalization c, a power-law disk flux $g(i)$, and a stellar companion flux $h(i)$:

$$F_{theory,i} = c * g(i) + h(i), \tag{3.3}$$

$$\chi^2 = \sum_i \left(\frac{F_{obs,i} - F_{theory,i}}{\sigma_i} \right)^2, \tag{3.4}$$

$$\frac{\partial \chi^2}{\partial c} = 0 = \sum_i 2 \left(\frac{F_{obs,i} - F_{theory,i}}{\sigma_i} \right) \left(-\frac{\partial F_{theory,i}}{\partial c} \right), \tag{3.5}$$

$$0 = \sum_i \left(\frac{F_{obs,i}}{\sigma_i^2} \right) * g(i) - \frac{c * g(i)^2}{\sigma_i^2} - \frac{h(i)g(i)}{\sigma_i^2}, \tag{3.6}$$

which, solving for c, gives

$$c = \frac{\sum_i \frac{F_{obs,i} g(i) - h(i)g(i)}{\sigma_i}}{\sum_i \frac{g(i)^2}{\sigma_i^2}}. \tag{3.7}$$

With this procedure, the results of the fitting process were obtained, given in Table 3.2. Several key results are obtained. If M15 X-3's optical magnitudes are fit to either a power-law accretion disk alone or a main-sequence companion alone, one obtains a reduced χ^2 of 8.87 and 16.89, respectively. The best fit for M15 X-3's optical counterpart is a combined spectrum, where M15 X-3's companion and its accretion disk both contribute in the optical bands. If both the normalization and the power-law index are allowed to vary, the obtained fit is overconstrained ($\chi^2 = 0.18$ for 0 degrees of freedom) and the inferred companion mass is $0.515^{+0.005}_{-0.270}\, M_\odot$. Note that for 0 degrees of freedom, there is no goodness of fit — we expect $\chi^2 = 0$ exactly. This model also has a best-fit power-law index of $\Gamma_\lambda = -4$, the Rayleigh-Jeans limit, but it is poorly constrained because the entire parameter space ($-4 < \Gamma_\lambda < -2$) is included in the 90% confidence interval. In general, fitting for both parameters gives a wide range of acceptable mass, index, and relative flux contributions. However, we have strong reason to believe that any accretion disk for this source would be in the conventional accretion disk regime, where $\Gamma_\lambda = -\frac{7}{3}$ (see Section 4.1). If the

index is constrained to be $\Gamma_\lambda = -\frac{7}{3}$, a fit with $\chi^2 = 0.44$ for 1 degree of freedom is obtained and gives a best fit mass of $0.440^{+0.035}_{-0.060}\ M_\odot$. Under this prescription, the accretion disk is the largest contributor to the system's flux in the bluer filters B_{438} and V_{606}. In the redder I_{814} filter, the disk and the companion are approximately equal in flux contribution. An accretion disk dominating emission at shorter wavelengths explains well why M15 X-3's optical counterpart appears much bluer than M15's main sequence.

Model	Γ_λ	$\frac{F_{disk}}{F_{total}}$			$M_{companion}$	χ^2/dof
		B_{438}	V_{606}	I_{814}		
(1)	no data	$[0]^A$	$[0]^A$	$[0]^A$	0.540 ± 0.005	33.78/2
(2)	$-2.00^{+0.00^C}_{-0.06}$	$[1]^B$	$[1]^B$	$[1]^B$	no data	8.87/1
(3)	$[-\frac{7}{3}]$	$0.87^{+0.07}_{-0.06}$	$0.68^{+0.13}_{-0.13}$	$0.53^{+0.15}_{-0.15}$	$0.440^{+0.035}_{-0.060}$	0.44/1
(4)	$-4.00^{+2.00^C}_{-0.00^C}$	$0.71^{+0.28}_{-0.07}$	$0.35^{+0.58}_{-0.03}$	$0.16^{+0.71}_{-0.01}$	$0.515^{+0.005}_{-0.270}$	0.18/0

Table 3.2: Results of fitting M15 X-3's optical magnitudes to various PYSYNPHOT models; (1) = Companion Only; (2) = Power-Law Only; (3) = Fixed Power-Law + Companion; (4) = Free Power-Law + Companion. Companion masses are given in $M_\odot$. Values in square brackets indicate a parameter that is held fixed. "No data" indicates that the parameter belongs to a model component that is absent in fitting. For "Companion only," (^{A}) the flux ratio is 0 since no disk is modelled, while for "Power-Law only" (^{B}) the flux ratio is 1 since only a disk is modelled. The error on the power-law index can hit one of its physically motivated boundaries (Γ_λ must be between -4 and -2) before reaching the edge of the confidence level; in such cases (^{C}), the index is unconstrained to that boundary with the error listed indicating the extent to that boundary. All error values are given at the 90% confidence level.

3.2.2 X-Ray Irradiation of the Companion

Although a main-sequence companion and accretion disk offers a reasonable explanation for M15 X-3's optical colours, it is worth considering whether the optical colours can also be explained by a low-mass companion being irradiated by the X-ray flux from the primary. If the X-ray flux is significant, it is possible that the companion would be hotter (and hence bluer) than a normal main-sequence star of the same size. In order for the X-ray flux to be significant, the bolometric flux from a portion of the companion's surface must be comparable to, or less than, the X-

ray flux impinging on the same portion. To determine if this is the case, consider a non-irradiated companion of mass $M_2 = 0.44\ M_\odot$ orbiting a 1.4 $M_\odot$ primary emitting 10^{34} erg s^{-1} of X-rays. This gives a mass ratio $q = \frac{M_2}{M_1}$ of ≈ 0.31. The binary separation can be given as [3]:

$$a = 3.5 \times 10^{10} (M_1)^{\frac{1}{3}} (1+q)^{\frac{1}{3}} (P_{hr})^{\frac{2}{3}} \text{ cm.} \tag{3.8}$$

For a lower main-sequence star filling its Roche Lobe, the period is approximately given by [3]:

$$M_2 \approx 0.11 P_{hr}, \tag{3.9}$$

which gives an orbital period of roughly 4 hours for M15 X-3. Substituting this relation in place of M_2 gives the orbital separation as:

$$a \simeq 3.5 \times 10^{10} M_1 (1+q)^{\frac{1}{3}} \left(\frac{M_2}{0.11}\right)^{\frac{2}{3}} \text{cm.} \tag{3.10}$$

For M15 X-3, this gives $a \sim 1.3 \times 10^{11}$ cm, meaning that the X-ray flux received by the companion at its surface is:

$$F_x \approx \frac{L_x}{4\pi a^2} = \frac{10^{34}\,\text{erg}\,\text{s}^{-1}}{4\pi (1.3 \times 10^{11}\text{cm})^2} = 3.5 \times 10^{10}\,\text{erg}\,\text{cm}^{-2}\,\text{s}^{-1}. \tag{3.11}$$

This value can be compared with the bolometric flux of M15 X-3's companion, which can be roughly estimated using a luminosity of $L_\bigstar \approx 0.05\ L_\odot$ and $R_\bigstar \approx 0.44$ $R_\odot$ for a 0.44 $M_\odot$ companion. Then, the flux of the companion at its surface is:

$$F_\bigstar \approx \frac{L_\bigstar}{4\pi R_\bigstar^2} = \frac{0.05(3.8 \times 33\,\text{erg}\,\text{s}^{-1})}{4\pi (0.44 \times 7.0 \times 10^{10}.\ \text{cm})^2} = 1.6 \times 10^{10}\,\text{erg}\,\text{cm}^{-2}\,\text{s}^{-1} \tag{3.12}$$

The X-ray flux on the portion of the companion's surface directly facing the accretor, by this analysis, is roughly a factor of 2 larger than the flux emitted by the companion. This means that X-ray irradiation can be significant in the observed flux

from M15 X-3 in the optical band, and the companion is most likely smaller than the calculated $0.440^{+0.035}_{-0.060}\,M_{\odot}$ obtained from the fit. One caveat is that if the companion is inefficient at absorbing X-rays, the effects of irradiation would be reduced. The mass of the companion can be constrained in a simple way by assuming that M15 X-3's companion re-radiates the X-ray flux it receives as a blackbody of temperature:

$$T_{irradiation} = \left(\frac{\sigma}{F_{\bigstar} + F_x}\right)^{\frac{1}{4}}. \tag{3.13}$$

If it is assumed that the radius of the star is given by [36]:

$$\left(\frac{R}{R_{\odot}}\right)^2 = \left(\frac{L}{L_{\odot}}\right)\left(\frac{T}{T_{\odot}}\right)^{-4}, \tag{3.14}$$

then modelling the star as a blackbody with radius R and temperature T permits the fitting procedure to be performed with blackbodies of varying temperatures and sizes on a grid to determine the maximum possible effect of irradiation. In a time-averaged sense, regardless of inclination, one expects that at most half of the visible star would be irradiated. In the maximal case, with an edge-on inclination, it is possible that the entirety of the observed face of the star is irradiated. This forms the maximally limiting case and is that considered in fits. Shown in Figure 3.4 are the results of fitting the magnitudes of M15 X-3 to a power-law accretion disk (index fixed) and a blackbody of varying size and temperature. Both the normal main-sequence and a maximally irradiated main-sequence (with the new temperature calculated using the above formulae applied to each star individually) are plotted over the contour. In the maximally irradiated case, the smallest acceptable star at the 3σ level is 0.15 $M_{\odot}$, which is useful for ruling out several explanations for VFXT behaviour (see Section 4.3).

3.2.3 Optical Conclusions

Before proceeding to the discussion of the results and further analysis plans, several conclusions about M15 X-3 can be made from the optical observations. Taken in

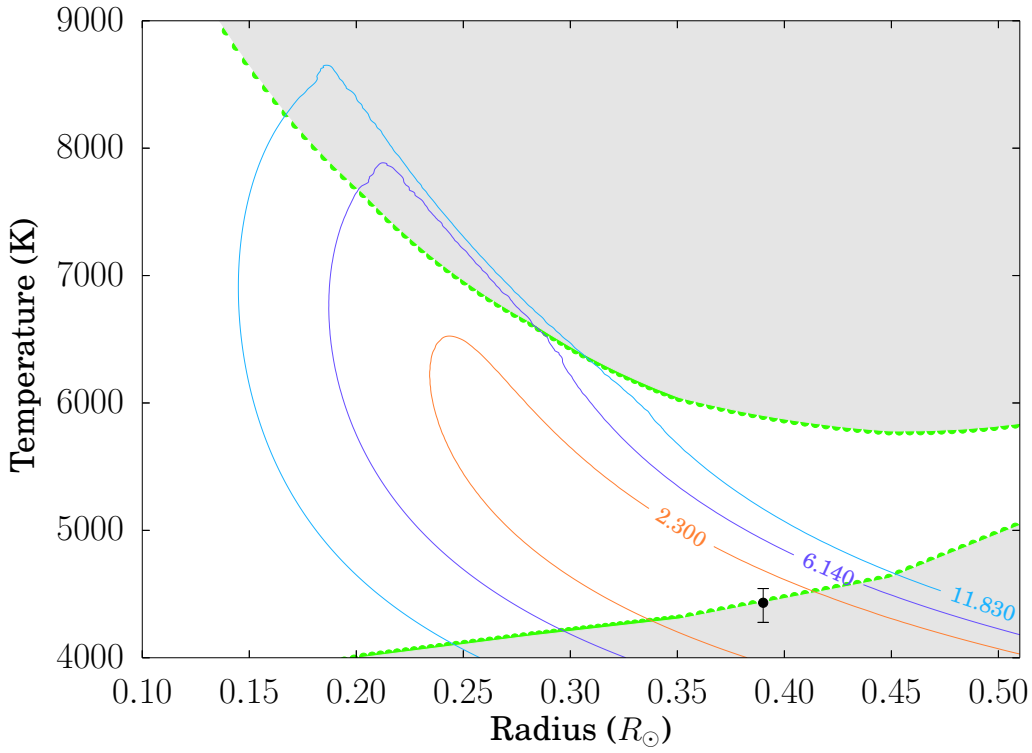

Figure 3.4: Contour plot of a fit of M15 X-3's magnitudes to a combined power-law (with fixed index at $\Gamma_\lambda = -\frac{7}{3}$) and blackbody. Here, instead of a star, a blackbody of size R (in $R_\odot$) and temperature T is used to investigate whether an irradiated star of much lower mass explains observations of M15 X-3. Since the blackbody has two parameters (compared with the 1 mass parameter of the star) the fitting is performed with 0 degrees of freedom, which implies that the best fit should be $\chi^2 = 0$. The 1σ, 2σ, and 3σ contours are plotted in orange, purple, and blue respectively for 2 degrees of freedom. The lower green curve represents the main sequence for low-mass stars of metallicity $[M/H] = -2.0$, ranging between 0.083 $M_\odot$and 0.70 $M_\odot$. The black point represents the best-fit and errors for the fixed power-law + normal stellar companion (third column in Table 3.2). The upper green curve represents the temperature and radius of main-sequence stars that have been irradiated by $10^{34}\,\mathrm{erg\,s^{-1}}$ of X-rays and maximally reradiate these as a blackbody. Grey regions of the plot are ruled out for physical reasons, as stars below the main-sequence curve would be too cold (for their radius), while stars above the irradiated main-sequence are hotter than possible given M15 X-3's X-ray flux from the primary.

tandem with the X-ray behaviour it shows:

1. M15 X-3 has a clear excess in bluer filters, and it lies off the main sequence in M15 in all filters, becoming increasingly away from the main sequence in bluer filters.

2. Fitting with a conventional accretion disk and lower main-sequence companion gives a best-fit mass of $0.440^{+0.035}_{-0.060}\,M_{\odot}$. While this is a relatively low mass star, it is significantly higher than suggested for most accretion scenarios for VFXTs.

3. Since the accretor's X-ray flux is comparable to the bolometric flux of the companion at its own surface, M15 X-3 is likely having its outgoing flux (and potentially its stellar evolution) altered by X-ray irradiation from the accretor. At the 3σ level, the smallest possible star that is acceptable with M15 X-3's observed magnitudes is $0.15\,M_{\odot}$.

Chapter 4

Discussion and Conclusions

4.1 Justification of the Accretion Disk Approximation

It is appropriate to consider whether the assumption that M15 X-3's accretion disk can be well-approximated by a power-law of index $\Gamma_\nu = \frac{1}{3}$ is reasonable. This condition is given by the following (see Section 1.1.3):

$$kT(R_{out})/h \ll \nu \ll kT_\star/h. \tag{4.1}$$

First we consider the optical band. The three wavebands used to study M15 X-3 are B_{438},V_{606}, and I_{814} (see Section 3.1.2), with central frequencies of 6.8×10^{14} Hz, 4.9×10^{14} Hz, and 3.7×10^{14} Hz, respectively. Our approximation is then valid if these frequencies are significantly higher than the characteristic frequency of the outer edge of the accretion disk, and significantly lower than the characteristic frequency of the inner edge of the accretion disk. For the inner edge of the accretion disk, we can calculate $T_\star$ with Equation 4.2, applying the additional assumptions of a $1.4M_\odot$ neutron star accretor of size $R_\star = 10^6 cm$, a $\approx 0.44M_\odot$ companion (this is the mass estimate determined for M15 X-3 in Section 3.2.1) and a mass transfer rate (onto the disk) of $\approx 10^{17}$ g s^{-1} (typical for neutron stars) [3].

$$T_\star = \left(\frac{3GM\dot{M}}{8\pi R_\star^3 \sigma}\right)^{1/4} \tag{4.2}$$

This then gives a temperature (for the above parameters) of $\approx 1.4 \times 10^7$ K and a frequency of $\approx 3 \times 10^{17}$ Hz, which is well above the frequencies of the optical bandpasses. For $R_{\rm out}$, a reasonable estimate of the outer accretion disk is the circularization radius $R_{\rm circ}$ (the radius at which material flowing through the Lagrange point assumes Keplerian circular orbits), given by [3]:

$$R_{circ} = a * (1+q)(0.500 - 0.227\log(q))^4. \tag{4.3}$$

In this case, $q = \frac{M_2}{M_1}$ is the mass ratio of the secondary to the primary and a is the binary separation derived from Kepler's law and conveniently given in the following form for an orbital period in hours P_{hr} [3]:

$$a = 3.5 \times 10^{10} (M_1)^{\frac{1}{3}} (1+q)^{\frac{1}{3}} (P_{hr})^{\frac{2}{3}} \text{ cm}. \tag{4.4}$$

For the above parameters, with the additional assumption that $P_{hr} \approx 4$ hrs for M15 X-3 (see section 3.2.2), one obtains $R_{circ} \simeq 2 \times 10^{10} cm$. At this radius, the temperature can be calculated from Equation 1.7 to be $\approx 8,000K$, which leads to a characteristic frequency of $\approx 1.7 \times 10^{14} Hz$. We can see that the lower limit of Equation 4.1 is true for the B and V filters, and less so for the I filter. This is not problematic since the I band contributes little information about the accretion disk as most of the flux there comes from the secondary. This analysis shows the disk spectrum should approach the Rayleigh-Jeans limit near the frequency of our I filter, such that a power-law fit in this regime should include the Rayleigh-Jeans limit in the range of acceptable indices.

4.2 Is M15 X-3 a Cluster Member?

Although the relative blueness of M15 X-3's optical counterpart suggests that it is a low-mass main sequence star in a system containing an accretion disk, it is reasonable to ask whether M15 X-3 might not be a member of the cluster. Since M15 X-3 emits in both X-rays and the optical wavelengths, there are two possibilities if M15 X-3 is not in the cluster:

1. M15 X-3 is a background active galactic nucleus (AGN). These regions, found in the centres of distant galaxies, sometimes contain strong X-ray emission that is generally believed to be the result of accretion onto the supermassive black hole located in the centre of these galaxies.

2. M15 X-3 is a foreground object, which would make it an intrinsically very faint star with strong X-ray emission.

The strongest argument against either a foreground or background object is the position of M15 X-3. Located only 20" away from the centre of one of the densest globular clusters in the Milky Way, it is extremely likely that it is located in the cluster. We can estimate the probability that this is an AGN by considering the number of expected hard X-ray sources (since M15 X-3 is a relatively hard X-ray source in its bright state) with the half-light radius around the centre of M15 ($r_h = 1.00'$ [37], $\omega = 8.7 \times 10^{-4}\,\mathrm{deg}^{-2}$). The number of hard X-ray sources (N) of flux $> S$ per area can be estimated from empirical relations found in Baldi et al. (2002) [38, 39, 40]. For M15 X-3, we use the bright state flux of $S \approx 5.6 \times 10^{-13}$ erg/(s cm^2), which gives an expected 0.6 sources per square degree, or 5×10^{-4} sources expected in the region where M15 X-3 was discovered (Note that the likelihood of finding a source at the distance of M15 X-3 from the GC centre is a factor of 9 smaller). This estimation makes it unlikely that M15 X-3 is a background source.

M15 X-3's position on the main sequence would also argue against a foreground source, since foreground stars tend to be redder than the main sequence of a globular

cluster. The first reason for this is that a foreground star would be intrinsically fainter (and hence lower-mass) than stars in the cluster. A lower-mass main-sequence star would then be colder, and hence, redder than a cluster member of the same apparent magnitude. Additional, the metallicity, when compared with the stars expected in the thin disk (where a foreground star would be most likely to lie, as the halo of the Milky Way is too sparsely populated with stars for it to be probable that it is located there), is extremely poor at $[M/H]$ of -2.0. Metal-poor stars tend to be hotter and more luminous than their metal-rich counterparts, as metals increase the opacity of stars, lowering their effective temperatures [41].

Based on these arguments, it is reasonable to conclude that M15 X-3 is a member of the cluster.

4.3 Nature of the M15 X-3 System

With the assumption that M15 X-3 is a cluster member, we require that the origin of its X-ray emission is due to binary evolution. For the compact object, there are three possibilities: white dwarf, neutron star, or black hole. A white dwarf accretor can easily be established as unlikely, and was indeed ruled out [19]. Cataclysmic variables (CVs - systems consisting of a white dwarf accreting from a main-sequence companion) generally do not exceed 10^{32} erg s^{-1} unless they possess strong magnetic fields (*intermediate polar* CVs) in which case they generally do not show the long-term variability characteristic of M15 X-3 [42, 43]. Additionally, M15 X-3 has a rather high X-ray-to-optical flux ratio, making a CV more unlikely because they output most of their power in the optical/UV bands.

It is also possible that M15 X-3 is a black hole accretor. However, radio observations of M15 X-3 would seem to argue against a black-hole accretor, at least viewed edge-on. If M15 X-3 is being viewed edge-on, this would cause it to be an accretion disk corona (ADC) source, and we would expect it to have an intrinsic luminosity of roughly 10^{36} erg s^{-1}. For a black hole at 10^{36} erg s^{-1} viewed edge-on, we would

expect a radio flux of roughly 10^{30} erg s^{-1}. At 10.3 kpc, this would give roughly 1 mJy at 6 GHz [44]. However, a survey of M15 (at an average frequency of 6 GHz), that included the region containing M15 X-3, detected no source at M15 X-3's location [45]. This observation was approximately simultaneous with the 2011 HRC observation, when M15 X-3 was active. With an rms sensitivity of 2.1 μJy/beam, a non-detection implies that any source at this position could be no brighter than 10.5 μJy at 5σ, much smaller than the flux density expected for an edge-on black hole. If a propeller effect is driving observed VFXT behaviour, then VFXTs should not be black holes, since they do not possess magnetic fields.

Additional information about the nature of the accretor can be obtained from the HRC observations of M15 X-3 in its quiescent state, which suggest a relatively soft spectrum in the quiescent state. These soft spectra imply the observation of a neutron star surface, which is also evidence against a black hole accretor [19]. If M15 X-3 is a neutron star accretor, this also makes it unlikely that the source is observed edge-on since the neutron star surface would not be visible at this inclination. In addition, a neutron star accretor observed edge-on would likely intrinsically produce at least 10^{36} erg/s. This would lead to an expected radio flux density of roughly 20 μJy at 6 GHz, also ruled out by the non-detection limit [46, 45].

Several of the proposed accretion scenarios described in Section 1.2.1 can be ruled out in the case of M15 X-3. If M15 X-3 was accreting from an extremely low-mass companion ($< 0.01 M_{\odot}$), either a primordial companion (planet or brown dwarf) or one that has been reduced to an extremely low-mass through mass transfer to the primary, we would expect that optical emission from the system should consist only of an accretion disk. However, as clearly shown in Section 3.2.1, a poor fit of a power-law alone to M15 X-3's observed optical flux implies that the accretion disk is not the only contributor to the system's optical flux. A companion of this mass producing the observed optical colours, even being maximally irradiated by the accretor, is unlikely. These companions would have sizes of $< 0.1 R_{\odot}$, which is clearly ruled out at the 3σ level by fitting to an irradiated blackbody 3.2.2.

An intermediate mass black hole (IMBH) accretor is also extremely unlikely in the case of M15 X-3 [22]. As mentioned above, M15 lies 20" away from the core of the cluster ($r_{\rm core}$ = 8"). We would expect that for an IMBH of size $\approx 1000 M_{\odot}$, it would sink to the centre of the cluster long on the timescale of dynamical friction, before the current epoch. A full treatment results in an infall timescale of [47, 48]:

$$t_{infall} = \frac{2\pi v_M r_i^2}{CGM}. \tag{4.5}$$

In this case, v_M is the initial velocity of the object of mass M which spirals into the cluster beginning from a radius r_i. C is a function that depends on the relative magnitudes of v_M and the velocity dispersion of the surrounding medium. For a typical globular cluster, $C \approx 76$. At the upper bound of this timescale, we take the velocity to be the escape velocity ($v_M = 43$ km/s) and the radius to be the tidal radius ($r_i = 61$) pc [49]. With these assumptions, we obtain a maximum possible sinking time of 3 Gyrs, which is small compared to the estimated 12 Gyr age of M15 [50]. This calculation argues that a proposed IMBH could not have been formed in M15. Instead, an externally formed IMBH would need to have been captured by M15 from the stellar halo more recently. Regardless, the large discrepancy between the sinking time and the current age of M15 makes such a scenario unfavourable.

An ultracompact system involving a neutron star primary and white dwarf secondary, suggested as a requirement to explain low accretion rates by ionizing the entire accretion disk, is also unlikely [24]. As with a brown dwarf or planetary companion, a white dwarf companion would not be visible at this distance from M15. Even very young, hot white dwarfs have a V magnitude that is too faint given that M15's distance modulus of 15 would put the upper edge of the white dwarf cooling sequence at an apparent magnitude of V $\approx$ 25 (see Figure 1.3). Since M15 X-3's optical colors are poorly described by accretion disk only scenario, this would seem to be inconsistent. In addition, the radius of the donor is constrained to be large enough in the case where it is irradiated, such that no ultracompact system is acceptable.

From the possible explanations for VFXT behaviour, it seems most likely that

M15 X-3 is a neutron star accretor with a main-sequence companion of size roughly $M_{companion} \approx 0.44 M_{\odot}$. Thus, the inefficient accretion onto the NS would likely be due to the propeller effect. Generally, the propeller effect is discussed in the context of pulsars, because they tend to have the sufficiently strong magnetic fields necessary for a propeller to occur [16]. If M15 X-3 is experiencing a propeller effect, it is possible that it may be a pulsar in a transitional stage given the persistent X-ray luminosity of M15 X-3 is within the regime that has been suggested as a transitional state for sources that switch between a emitting as a millisecond pulsar (MSP) and as a bright low-mass X-ray binary [51, 52, 53, 54, 55].

4.4 Duty Cycle and Spectral Curvature

With the information provided by M15 X-3's long term light curve, (Section 2.2.2 and Figure 2.5) it is possible to estimate the duty cycle of the source, and hence infer a time-averaged accretion rate, so that both can be compared to other VFXTs. Several assumptions are made in order to estimate these quantities:

1. We assume that in the ≈ 20 years of X-ray observations presented in Figure 2.5, there are two periods where M15 X-3 is actively accreting, with one period of quiescence separating the two active periods. We also assume that this is representative of a single transient cycle of M15 X-3, namely that the derived time of active accretion is that of a single cycle. Although this is likely an underestimation of M15 X-3's bright time, more detailed assumptions are beyond the scope of this work.

2. We assume that the period M15 X-3 spends in either state is of order years. The minimum time spent in a quiescence state is given by the duration between the quiescent observations in ~ 2000 — 2002. The maximal quiescence time is given by the duration between the two observations on either side of the quiescent observations, namely ~ 1996 and ~ 2004.

3. We then assume that the true quiescent period can be estimated by a uniform distribution between these two extrema.

Under these assumptions, we estimate t_{faint} to be 5.0 ± 2.3 years (or $1.8 \pm 0.8 \times 10^3$ days). With a total observing period of 17.8 years, we estimate t_{bright} to be 12.8 ± 2.3 years (or $1.8 \pm 0.8 \times 10^3$ days).

The duty cycle is then given, rather simply, by:

$$DC = 1 - \frac{t_{faint}}{t_{total}}. \tag{4.6}$$

This gives a duty cycle of $72 \pm 13\%$, which is very high amongst VFXTs [56]. From this, the time-averaged luminosity can be estimated as:

$$\bar{L}_x = DC \times L_{bright} + (1 - DC) \times L_{faint}. \tag{4.7}$$

If we approximate M15 X-3's $L_{bright} \approx 8 \times 10^{33}$ erg s^{-1} and $L_{faint} \approx 10^{31}$ erg s^{-1} (based on the results in Table 2.1) then $\bar{L}_x = 5.8 \pm 1.0 \times 10^{33}$ erg s^{-1}. From this, the time-averaged accretion rate can be estimated as [3]:

$$\dot{M} = \frac{R_\star L_{acc}}{GM}. \tag{4.8}$$

This equation assumes that 100% of the kinetic energy of infalling material onto the neutron star is converted to X-rays (including emission from the heated NS and the accretion disk). Here, we additionally assume the canonical neutron star mass $M = 1.4 M_\odot$ and radius $R_\star = 10 km$. This gives a time-averaged accretion rate of $\dot{M} = 5.0 \pm 0.5 \times 10^{13}$ g s^{-1} or $\approx 5.0 \pm 0.9 \times 10^{-13} M_\odot$/yr.

Based on this analysis, M15 X-3's duty cycle makes it distinct from the short ($\lesssim$ 10%) duty cycle VFXTs, but its spectral features do not resemble other persistently bright VFXTs. The persistent VFXTs tend to have relatively soft power-law fits of $\Gamma \gtrsim 2$, or harder power-law fits if a thermal component is added [27]. By contrast, analysis of M15 X-3's spectra suggests that it lacks a thermal component, and it has

a rather hard power law index when fitted with a single power-law $\Gamma = 1.42 \pm 0.03$. This behaviour more closely resembles what is observed in bright LMXBs (those of $L_x \approx 10^{36}$). Absorption effects suppressing lower-energy X-rays are unlikely in this case, since the column density is only $4.6 \times 10^{20}\,\mathrm{cm}^{-2}$ in the direction of M15. Additionally, the lack of improved fitting in X-rays (Section 2.1.4) with N_H as a free parameter and other arguments (Section 4.3) suggest that M15 X-3 is not an intrinsically bright source being viewed edge-on.

The unusual observed broken power-law shape is difficult to motivate physically. Since fits of physically motivated models (power-law + thermal) are unable to explain this curvature, caution must be taken in interpreting this phenomenological fit. It is possible that a single comptonization model of low temperature and high optical depth could explain this turnover. However, in general, the quality of the data makes it unlikely that these parameters could be physically constrained. In addition, the parameters of comptonization models would be difficult to motivate on physical grounds.

4.5 Future Work

Further observations of M15 X-3 would provide additional constraints on the nature of the M15 X-3 system. There are three observations, which should be considered to provide valuable information on the source.

1. Although the measured optical magnitudes of M15 X-3 constrain it to be a relatively low-mass star, the best way to identify the companion would be to collect infrared photometry of the source. Unfortunately, the field near M15 X-3 is very crowded, which would make obtaining this data challenging with most instruments. However, IR photometery with *HST* (using the IR channel) or a ground-based telescope with adaptive optics, such as *Gemini* or the *Very Large Telescope* (VLT), would make such an observation possible, helping to determine the spectral class of the companion, and possibly estimating the

extent of X-ray irradiation by the primary.

2. If M15 X-3 is a source in a transitionary state between LMXB and MSP behaviour, this would imply that M15 X-3's quiescent state should demonstrate the radio emission expected from pulsars. A series of short X-ray observations to determine if M15 X-3 is in quiescence, followed by radio observation in quiescence, would confirm its pulsar nature. This would be extremely useful in resolving M15 X-3's unusual behaviour.

3. If M15 X-3 is a neutron star accretor, as we expect, then we expect that we should be able to observe the surface of the neutron star in quiescence. However, M15 X-3 has not been observed in quiescence by an instrument with sufficient spectral resolution for a sufficiently long period of time to definitively confirm this. Therefore, a long X-ray observation of M15 X-3 with *Chandra* ACIS when it is known to be in quiescence would be able to confirm that the neutron star surface has been observed, possibly even measuring its surface temperature.

4.6 Conclusions

In summary, we have presented the first combined optical/X-ray observation of a very faint X-ray transient (VFXT). At the time of the observations, M15 X-3 was in its "bright" state at a luminosity of $\approx 8 \times 10^{33}$ erg/s. The X-ray spectrum of M15 X-3, observed with *Chandra*, shows unusual curvature that is difficult to explain physically. It is best described as a power law of photon index $\Gamma = 1.28 \pm 0.06$ up to a break energy of $2.7^{+0.3}_{-0.6}$ keV, after which it is described as a power law of photon index $\Gamma = 1.9 \pm 0.2$. Optical observations with *HST* clearly detect an optical counterpart that is significantly bluer than the main sequence of M15, due to contributions from a low-mass companion and a power-law-like accretion disk. We find that X-ray irradiation is not negligible in the case of this source, and as such the

mass estimate of size $0.440^{+0.035}_{-0.060} M_{\odot}$ is likely an upper bound. However, we can rule out several proposed explanations for VFXT behaviour in the case of this source, as the companion cannot be of extremely low mass (constrained to be above 0.15 $M_{\odot}$ at 3σ). From this, we infer that M15 X-3 is most likely a neutron star XRB accreting inefficiently due to a propeller effect, and that it is possibly a transitional source between a bright LMXB and an MSP. We encourage continued observations of this source in the radio, X-ray, and optical to infared bands to further constrain its true nature.

Bibliography

[1] W. H. G. Lewin, J. van Paradijs, and E. P. J. van den Heuvel. *X-ray Binaries*. January 1997.

[2] R. Giacconi, H. Gursky, E. Kellogg, E. Schreier, and H. Tananbaum. Discovery of Periodic X-Ray Pulsations in Centaurus X-3 from UHURU. *ApJL*, 167:L67, July 1971. doi: 10.1086/180762.

[3] J. Frank, A. King, and D. J. Raine. *Accretion Power in Astrophysics: Third Edition*. January 2002.

[4] J. P. Lasota. The disc instability model of dwarf novae and low-mass X-ray binary transients. *New A Rev.*, 45:449–508, June 2001. doi: 10.1016/S1387-6473(01)00112-9.

[5] S. A. Balbus and J. F. Hawley. Instability, turbulence, and enhanced transport in accretion disks. *Reviews of Modern Physics*, 70:1–53, January 1998. doi: 10.1103/RevModPhys.70.1.

[6] C. Done, M. Gierliński, and A. Kubota. Modelling the behaviour of accretion flows in X-ray binaries. Everything you always wanted to know about accretion but were afraid to ask. *A&A Rev.*, 15:1–66, December 2007. doi: 10.1007/s00159-007-0006-1.

[7] J. van Paradijs. On the Accretion Instability in Soft X-Ray Transients. *ApJL*, 464:L139, June 1996. doi: 10.1086/310100.

[8] S. Campana, M. Colpi, S. Mereghetti, L. Stella, and M. Tavani. The neutron stars of Soft X-ray Transients. *A&A Rev.*, 8:279–316, 1998. doi: 10.1007/s001590050012.

[9] P. G. Jonker, R. Wijnands, and M. van der Klis. The faint neutron star soft X-ray transient SAX J1810.8-2609 in quiescence. *MNRAS*, 349:94–98, March 2004. doi: 10.1111/j.1365-2966.2004.07455.x.

[10] G. W. Clark. X-ray binaries in globular clusters. *ApJL*, 199:L143–L145, August 1975. doi: 10.1086/181869.

[11] F. Verbunt and W. H. G. Lewin. *Globular cluster X-ray sources*, pages 341–379. April 2006.

[12] L. M. Krauss and B. Chaboyer. Age Estimates of Globular Clusters in the Milky Way: Constraints on Cosmology. *Science*, 299:65–70, January 2003. doi: 10.1126/science.1075631.

[13] K. A. Woodley, R. Goldsbury, J. S. Kalirai, H. B. Richer, P.-E. Tremblay, J. Anderson, P. Bergeron, A. Dotter, L. Esteves, G. G. Fahlman, B. M. S. Hansen, J. Heyl, J. Hurley, R. M. Rich, M. M. Shara, and P. B. Stetson. The Spectral Energy Distributions of White Dwarfs in 47 Tucanae: The Distance to the Cluster. *AJ*, 143:50, February 2012. doi: 10.1088/0004-6256/143/2/50.

[14] J. Goodman and P. Hut. Primordial binaries and globular cluster evolution. *Nature*, 339:40–42, May 1989. doi: 10.1038/339040a0.

[15] H. B. Richer, R. Goldsbury, J. Heyl, J. Hurley, A. Dotter, J. S. Kalirai, K. A. Woodley, G. G. Fahlman, R. M. Rich, and M. M. Shara. Comparing the White Dwarf Cooling Sequences in 47 Tuc and NGC 6397. *ApJ*, 778:104, December 2013. doi: 10.1088/0004-637X/778/2/104.

[16] A. F. Illarionov and R. A. Sunyaev. Why the Number of Galactic X-ray Stars Is so Small? *A&A*, 39:185, February 1975.

[17] C. R. D'Angelo and H. C. Spruit. Accretion discs trapped near corotation. *MNRAS*, 420:416–429, February 2012. doi: 10.1111/j.1365-2966.2011.20046.x.

[18] M. M. Romanova, G. V. Ustyugova, A. V. Koldoba, and R. V. E. Lovelace. The Propeller Regime of Disk Accretion to a Rapidly Rotating Magnetized Star. *ApJL*, 616:L151–L154, December 2004. doi: 10.1086/426586.

[19] C. O. Heinke, H. N. Cohn, and P. M. Lugger. The Discovery of a Very Faint X-Ray Transient in the Globular Cluster M15. *ApJ*, 692:584–593, February 2009. doi: 10.1088/0004-637X/692/1/584.

[20] N. Degenaar and R. Wijnands. The behavior of subluminous X-ray transients near the Galactic center as observed using the X-ray telescope aboard Swift. *A&A*, 495:547–559, February 2009. doi: 10.1051/0004-6361:200810654.

[21] R. Wijnands, J. J. M. in't Zand, M. Rupen, T. Maccarone, J. Homan, R. Cornelisse, R. Fender, J. Grindlay, M. van der Klis, E. Kuulkers, C. B. Markwardt, J. C. A. Miller-Jones, and Q. D. Wang. The XMM-Newton/Chandra monitoring campaign of the Galactic center region. Description of the program and preliminary results. *A&A*, 449:1117–1127, April 2006. doi: 10.1051/0004-6361:20054129.

[22] A. R. King and R. Wijnands. The faintest accretors. *MNRAS*, 366:L31–L34, February 2006. doi: 10.1111/j.1745-3933.2005.00126.x.

[23] M. P. Muno, J. R. Lu, F. K. Baganoff, W. N. Brandt, G. P. Garmire, A. M. Ghez, S. D. Hornstein, and M. R. Morris. A Remarkable Low-Mass X-Ray Binary within 0.1 Parsecs of the Galactic Center. *ApJ*, 633:228–239, November 2005. doi: 10.1086/444586.

[24] J. J. M. in't Zand, R. Cornelisse, and M. Méndez. On the nature of two low-dot{M} X-ray bursters: 1RXS J170854.4-321857 and 1RXS J171824.2-

402934. *A&A*, 440:287–293, September 2005. doi: 10.1051/0004-6361:20052955.

[25] R. van den Bosch, T. de Zeeuw, K. Gebhardt, E. Noyola, and G. van de Ven. The Dynamical Mass-to-Light Ratio Profile and Distance of the Globular Cluster M15. *ApJ*, 641:852–861, April 2006. doi: 10.1086/500644.

[26] C. O. Heinke, G. B. Rybicki, R. Narayan, and J. E. Grindlay. A Hydrogen Atmosphere Spectral Model Applied to the Neutron Star X7 in the Globular Cluster 47 Tucanae. *ApJ*, 644:1090–1103, June 2006. doi: 10.1086/503701.

[27] M. Armas Padilla, N. Degenaar, and R. Wijnands. The X-ray spectral properties of very-faint persistent neutron star X-ray binaries. *MNRAS*, 434:1586–1592, September 2013. doi: 10.1093/mnras/stt1114.

[28] R. Janulis. Interstellar reddening in the direction of the globular cluster M15. *Baltic Astronomy*, 1:25, January 1992.

[29] M. P. Muno, E. Pfahl, F. K. Baganoff, W. N. Brandt, A. Ghez, J. Lu, and M. R. Morris. An Overabundance of Transient X-Ray Binaries within 1 Parsec of the Galactic Center. *ApJL*, 622:L113–L116, April 2005. doi: 10.1086/429721.

[30] M. Sakano, R. S. Warwick, A. Decourchelle, and Q. D. Wang. Unusual X-ray transients in the Galactic Centre. *MNRAS*, 357:1211–1218, March 2005. doi: 10.1111/j.1365-2966.2005.08717.x.

[31] D. Porquet, N. Grosso, V. Burwitz, I. L. Andronov, B. Aschenbach, P. Predehl, and R. S. Warwick. Discovery of a bright X-ray transient in the Galactic Center with XMM-Newton. *A&A*, 430:L9–L12, January 2005. doi: 10.1051/0004-6361:200400117.

[32] M. Del Santo, L. Sidoli, S. Mereghetti, A. Bazzano, A. Tarana, and P. Ubertini. XMMU J174716.1-281048: a "quasi-persistent" very faint X-ray transient? *A&A*, 468:L17–L20, June 2007. doi: 10.1051/0004-6361:20077536.

[33] A. Fruchter and et al. *HST MultiDrizzle Handbook*. January 2009.

[34] I. Baraffe, G. Chabrier, F. Allard, and P. H. Hauschildt. Evolutionary models for metal-poor low-mass stars. Lower main sequence of globular clusters and halo field stars. *A&A*, 327:1054–1069, November 1997.

[35] F. Castelli and R. L. Kurucz. New Grids of ATLAS9 Model Atmospheres. *ArXiv Astrophysics e-prints*, May 2004.

[36] C. J. Hansen, S. D. Kawaler, and V. Trimble. *Stellar interiors : physical principles, structure, and evolution*. 2004.

[37] W. E. Harris. Globular Clusters in the Milky Way (Harris, 1996). *VizieR Online Data Catalog*, 7195:0, November 1996.

[38] A. Baldi, S. Molendi, A. Comastri, F. Fiore, G. Matt, and C. Vignali. The HELLAS2XMM Survey. I. The X-Ray Data and the logN-logS Relation. *ApJ*, 564:190–195, January 2002. doi: 10.1086/324261.

[39] P. Giommi, M. Perri, and F. Fiore. The BeppoSAX 2-10 keV survey. *A&A*, 362:799–808, October 2000.

[40] Y. Ueda, T. Takahashi, H. Inoue, T. Tsuru, M. Sakano, Y. Ishisaki, Y. Ogasaka, K. Makishima, T. Yamada, M. Akiyama, and K. Ohta. LOG N-LOG S Relations and Spectral Properties of Sources from the ASCA Large Sky Survey: Their Implications for the Origin of the Cosmic X-Ray Background (CXB). *ApJ*, 518:656–671, June 1999. doi: 10.1086/307291.

[41] L. S. Sparke and J. S. Gallagher, III. *Galaxies in the Universe: An Introduction*. Cambridge University Press, 2007.

[42] D. S. Baskill, P. J. Wheatley, and J. P. Osborne. The complete set of ASCA X-ray observations of non-magnetic cataclysmic variables. *MNRAS*, 357:626–644, February 2005. doi: 10.1111/j.1365-2966.2005.08677.x.

[43] M. P. Muno, J. S. Arabadjis, F. K. Baganoff, M. W. Bautz, W. N. Brandt, P. S. Broos, E. D. Feigelson, G. P. Garmire, M. R. Morris, and G. R. Ricker. The Spectra and Variability of X-Ray Sources in a Deep Chandra Observation of the Galactic Center. *ApJ*, 613:1179–1201, October 2004. doi: 10.1086/423164.

[44] E. Gallo, B. P. Miller, and R. Fender. Assessing luminosity correlations via cluster analysis: evidence for dual tracks in the radio/X-ray domain of black hole X-ray binaries. *MNRAS*, 423:590–599, June 2012. doi: 10.1111/j.1365-2966.2012.20899.x.

[45] J. Strader, L. Chomiuk, T. J. Maccarone, J. C. A. Miller-Jones, A. C. Seth, C. O. Heinke, and G. R. Sivakoff. No Evidence for Intermediate-mass Black Holes in Globular Clusters: Strong Constraints from the JVLA. *ApJL*, 750: L27, May 2012. doi: 10.1088/2041-8205/750/2/L27.

[46] S. Migliari and R. P. Fender. Jets in neutron star X-ray binaries: a comparison with black holes. *MNRAS*, 366:79–91, February 2006. doi: 10.1111/j.1365-2966.2005.09777.x.

[47] J. Binney and S. Tremaine. *Galactic Dynamics: Second Edition*. Princeton University Press, 2008.

[48] B. W. Carroll and D. A. Ostlie. *An introduction to modern astrophysics and cosmology*. July 2006.

[49] C. J. Peterson and I. R. King. The structure of star clusters. VI. Observed radii and structural parameters in globular clusters. *AJ*, 80:427–436, June 1975. doi: 10.1086/111759.

[50] M. Koleva, P. Prugniel, P. Ocvirk, D. Le Borgne, and C. Soubiran. Spectroscopic ages and metallicities of stellar populations: validation of full spectrum fitting. *MNRAS*, 385:1998–2010, April 2008. doi: 10.1111/j.1365-2966.2008.12908.x.

[51] N. Degenaar, R. Wijnands, M. T. Reynolds, J. M. Miller, D. Altamirano, J. Kennea, N. Gehrels, D. Haggard, and G. Ponti. The peculiar Galactic center neutron star X-ray binary XMM J174457-2850.3. *ArXiv e-prints*, June 2014.

[52] A. Papitto, C. Ferrigno, E. Bozzo, N. Rea, L. Pavan, L. Burderi, M. Burgay, S. Campana, T. di Salvo, M. Falanga, M. D. Filipović, P. C. C. Freire, J. W. T. Hessels, A. Possenti, S. M. Ransom, A. Riggio, P. Romano, J. M. Sarkissian, I. H. Stairs, L. Stella, D. F. Torres, M. H. Wieringa, and G. F. Wong. Swings between rotation and accretion power in a binary millisecond pulsar. *Nature*, 501:517–520, September 2013. doi: 10.1038/nature12470.

[53] A. M. Archibald, I. H. Stairs, S. M. Ransom, V. M. Kaspi, V. I. Kondratiev, D. R. Lorimer, M. A. McLaughlin, J. Boyles, J. W. T. Hessels, R. Lynch, J. van Leeuwen, M. S. E. Roberts, F. Jenet, D. J. Champion, R. Rosen, B. N. Barlow, B. H. Dunlap, and R. A. Remillard. A Radio Pulsar/X-ray Binary Link. *Science*, 324:1411–, June 2009. doi: 10.1126/science.1172740.

[54] S. Bogdanov, A. Patruno, A. M. Archibald, C. Bassa, J. W. T. Hessels, G. H. Janssen, and B. W. Stappers. X-Ray Observations of XSS J12270-4859 in a New Low State: A Transformation to a Disk-free Rotation-powered Pulsar Binary. *ApJ*, 789:40, July 2014. doi: 10.1088/0004-637X/789/1/40.

[55] C. G. Bassa, A. Patruno, J. W. T. Hessels, E. F. Keane, B. Monard, E. K. Mahony, S. Bogdanov, S. Corbel, P. G. Edwards, A. M. Archibald, G. H. Janssen, B. W. Stappers, and S. Tendulkar. A state change in the low-mass X-ray binary XSS J12270-4859. *MNRAS*, 441:1825–1830, June 2014. doi: 10.1093/mnras/stu708.

[56] N. Degenaar, R. Wijnands, E. M. Cackett, J. Homan, J. J. M. in't Zand, E. Kuulkers, T. J. Maccarone, and M. van der Klis. A four-year XMM-Newton/Chandra monitoring campaign of the Galactic centre: analysing the

X-ray transients. *A&A*, 545:A49, September 2012. doi: 10.1051/0004-6361/201219470.